Article

Seawater Intrusion Risk and Prevention Technology of Coastal and Large-Span Underground Oil Storage Cavern

Shengquan He [1,2], **Dazhao Song** [1,2,*], **Lianzhi Yang** [1,2], **Xiaomeng Miao** [3], **Jiuzheng Liang** [4], **Xueqiu He** [1,2], **Biao Cao** [1,2], **Yingjie Zhao** [1,2], **Tuo Chen** [5], **Wei Zhong** [4] and **Taoping Zhong** [1,2]

1   Key Laboratory of Ministry of Education for Efficient Mining and Safety of Metal Mine, University of Science and Technology Beijing, Beijing 100083, China
2   Research Institute of Macro-Safety Science, University of Science & Technology Beijing, Beijing 100083, China
3   Sinochem Energy Logistics Co., Ltd., Beijing 100031, China
4   China Petroleum Pipeline Engineering Co., Ltd., Langfang 065000, China
5   Department of Mining and Materials Engineering, McGill University, Montreal, QC H3A 0E8, Canada
*   Correspondence: song.dz@163.com; Tel.: +86-185-1513-9977

Abstract: The presence of a high concentration of Cl^- in saltwater will erode the structure and facilities, reducing the stability and service life of the underground oil storage cavern. In order to reduce the risk of seawater intrusion, this paper studies the risk and prevention technology of seawater intrusion based on a case study of a coastal and large-span underground oil storage cavern. A refined three-dimensional hydrogeological model that comprehensively considers permeability coefficient partitions, faults, and fractured zones are constructed. The seepage fields and seawater intrusion risks of the reservoir site in its natural state, during construction, and during operation are examined, respectively. The study quantifies the water inflow and optimizes the seawater intrusion prevention technology. The results indicate that there is no risk of seawater incursion into the cavern under natural conditions. The water inflows after excavating the top, middle, and bottom sections of the main cavern are predicted to be 6797 m^3/day, 6895 m^3/day, and 6767 m^3/day, respectively. During the excavation period, the water supply from the water curtain system is lower than the water inflow of the cavern, providing the maximum water curtain injection of 6039 m^3/day. The water level in the reservoir area decreased obviously in the excavation period, but the water flow direction is from the cavern to the sea. Additionally, the concentration of Cl^- in the cavern area is less than 7 mol/m^3; hereby, there are no seawater intrusion risks. When only the horizontal water curtain system is deployed, seawater intrusion occurs after 18 years of cavern operation. The concentration of Cl^- in the southeast of the cavern group exceeds 50 mol/m^3 in 50 years, reaching moderate corrosion and serious seawater intrusion. In addition to the horizontal curtain above the cavern, a vertical water curtain system could be added on the southeast side, with a borehole spacing of 10 m and extending to 30 m below the cavern group. This scheme can effectively reduce seawater intrusion risk and extend the service life of the cavern. The findings of this research can be applied as guidelines for underground oil storage caverns in coastal areas to tackle seawater intrusion problems.

Keywords: cavern group; seepage field; solute transport field; water inflow; water curtain system

1. Introduction

Petroleum, as an important strategic resource, is unevenly distributed among different regions. Up to 70.9% of China's crude oil depends on imports; therefore, building up large-scale oil reserves is essential to ensuring national energy security [1]. Because underground oil storage has advantages such as low cost, high safety and minimal footprint, it has grown to be an important method for oil storage [2]. The vast majority of underground oil storage caverns in the world are constructed in freshwater regions with good rock integrity and far away from the coastline [3,4], but such ideal sites are scarce [5]. The construction of underground oil storage caverns on islands with favorable geological conditions can

encourage not only the utilization of island resources but also facilitate the storage of imported crude oil [6]. When underground oil storage caverns are close to seawater, there is a problem of seawater intrusion during excavation and operation. Seawater contains harmful substances such as Cl^- with a high concentration that pollutes crude oil, corrodes underground structural facilities, and reduces the long-term stability and service life of underground oil storage caverns [7,8]. Therefore, it is necessary to study the seawater intrusion problems of underground oil storage caverns.

Kim et al. [9] and Jo et al. [10] characterized the degree of seawater intrusion by the concentration of Cl^- and concluded that different levels of seawater intrusion would occur during the construction and operation of underground oil storage cavern. By taking Yeosu underground oil storage cavern in South Korea as a case study, Lim et al. [11] analyzed the risk of seawater intrusion into coastal underground oil storage caverns through fractured bedrocks using hydrogeochemical and isotopic indicators and concluded that site hydrogeology heterogeneity is the main reason for the difference of seawater intrusion at different locations in the reservoir area. Lee et al. [12] concluded that storage location, seepage water flow rate, and fracture zones are important factors affecting the temporal and spatial variation in Cl^- concentration in a coastal underground oil storage cavern through on-site monitoring and numerical simulation. Park et al. [13] concluded that underground mining plays a major role in seawater intrusion into fractured bedrock aquifers, which is affected by the type and hydraulic conductivity of water-conducting fractures through long-term monitoring, time-dependent analysis, and hydraulic test. Li et al. [14] established a three-dimensional model of a large underground oil storage cavern using the equivalent continuum method. The anisotropic permeability tensor of fractured rock mass and field data are used to predict the underground water level change in different construction stages. Cui et al. [15] analyzed the seepage characteristics of porous rock mass and fissures in an underground water-sealed cavern and introduced unsaturated seepage flow characteristics for the calculation of water inflow. The formula of soil and water characteristic curve was also introduced into finite element calculation to achieve dynamic water inflow calculation during cavern excavation. Kharroubi et al. [16] analyzed the distribution of groundwater in southern Tunisia and concluded that groundwater salinization might be related to the infiltration of seawater through faults. Papadopoulou et al. [17] established a subsurface flow and contaminant transport model and concluded that the connectivity of the fractures and the fluid density effects are important factors that drive seawater intrusion. Despina et al. [18] studied the transient electromagnetic soundings data and concluded that saline water intrusion might occur along the fractures of the fault zone. Yan et al. [19] and Wang et al. [20] used Midas software to establish a fault model and conduct simulation research.

A water curtain system is a method to increase the freshwater momentum by injecting freshwater around the underground cavern to supplement the loss of groundwater caused by cavern excavation and alleviate the decline of the groundwater level. This is a technique to prevent seawater intrusion. Huyakorn et al. [21] found that when the water flow in the underground cavern exceeds the underground fresh supply water quantity from the water curtain system, the freshwater head drops. Once the freshwater head is lower than the seawater head, the freshwater–seawater interface will push inland, resulting in seawater intrusion. Shi et al. [6] analyzed the autocorrelation and cross-correlation among water inflow, water curtain system injection pressure, and underground water level during the construction of an underground oil storage cavern. They concluded that the efficiency of the water curtain system is affected by rainfall and rock quality near the reservoir area. Liu et al. [22] investigated the interaction between the system parameters of the water curtain system and the geometrical parameters of the rock fracture. A closed efficiency evaluation method from the perspective of system parameter optimization is proposed and applied to a reservoir. Qiu et al. [23] analyzed the field time series data of offshore underground oil reserves, the long-term and short-term memory models are used to predict the seepage field in the reservoir area, which provides the reference for the performance

optimization of the water screen system. Li et al. [24] analyzed the dynamic characteristics of seawater intrusion in the underground oil storage cavern under a tidal environment based on the theory of multi-physical field coupling and the finite element method. It was concluded that the water curtain system plays an important role in inhibiting seawater intrusion. Wang et al. [25] studied the groundwater response to a water curtain system of an oil storage cavern through on-site monitoring and statistical analysis and concluded that the response is related to the facility's geometric layout and hydrogeology. The water curtain system injected water and raised the underground water level [26,27]. Dai et al. [28] and Li et al. [29] studied the seepage characteristics and water inflow of the underground oil storage cavern and evaluated the design parameters of the water curtain system, such as width, water pressure, hole spacing, and elevation. The seepage field and water inflow during the operation were evaluated. Xu et al. [30] studied the variation in water inflow and seepage field with different water curtain system parameters through numerical simulation and proposed the concept of minimum water inflow to design a water curtain system. Xue et al. [31] simulated the seepage characteristics of the water curtain system by the finite-element model based on the concept of the minimum seepage pressure, and they found that excessive water curtain pressure causes the groundwater velocity and water head increase around the reservoir.

Although extensive research has been conducted on seawater intrusion issues, few literatures are found to be related to seawater intrusion in the underground oil storage cavern close to the coastline, especially ones with faults and the densely fractured zone around the reservoir area. In order to fill the gap, this study constructs a fine three-dimensional hydrogeological model based on a typical coastal and large-span underground oil storage cavern project. The model comprehensively considers variables such as faults, dense joint zones, land use types, and permeability variation in different regions. The evolution rules of the seepage field and Cl^- concentration field are examined in their natural state, during construction, and during the operation of the reservoir. The water inflow, supply water amount, and the inhibition of the water curtain system on seawater intrusion are all analyzed. The findings of the study can be used to resolve saltwater intrusion problems when developing underground oil storage caverns in coastal locations.

2. Engineering Background

2.1. Project Overview

The studied underground oil storage cavern group is located in the littoral area, with 11 oil storage caverns. The expected service life is 50 years. The cavern spacing is 30.8 m, and the section size is 22×30 m. The top and bottom elevations of the oil storage cavern are -62 m and -92 m, respectively. The buried depth of the cavern is between 92 and 212 m below the ground surface. A horizontal water curtain system is set 25 m above the oil storage cavern, with a water curtain hole spacing of 10 m. Moreover, a vertical water curtain system with a water curtain hole spacing of 10 m extending to 30 m below the cavern is set around the cavern group.

2.2. Engineering Geology

The surface layer of the reservoir area is mostly quaternary residual slope soil. The bedrock is mainly consisting of monzogranite invaded by late Yanshanian magma in the eastern, gabbro invaded by late Yanshanian magma in the center, and predevonian gneisses granite in the western. The surrounding rock mass of the cavern ground is dominantly first-grade and second-grade. The faults revealed by geological exploration around the reservoir include NE-trending faults F1, F2, F3, and F16; NW-trending faults F7 and F18; NWW-trending faults F8; near EW-trending faults F9, F12, F15, and F17; and NNE-trending faults F10, F11, F13, and F14. Relevant data of the above 14 faults are from the exploration results in the feasibility stage of the project. The distribution of seven continuous densely jointed zones (WJ1–WJ7) and fourteen faults are delineated in Figure 1. Among them, F1 in

the east and F8 in the south of the cavern has a great influence on the hydrogeology of the reservoir area. The bandwidths of F1 and F8 are 30 m and 5 m, respectively.
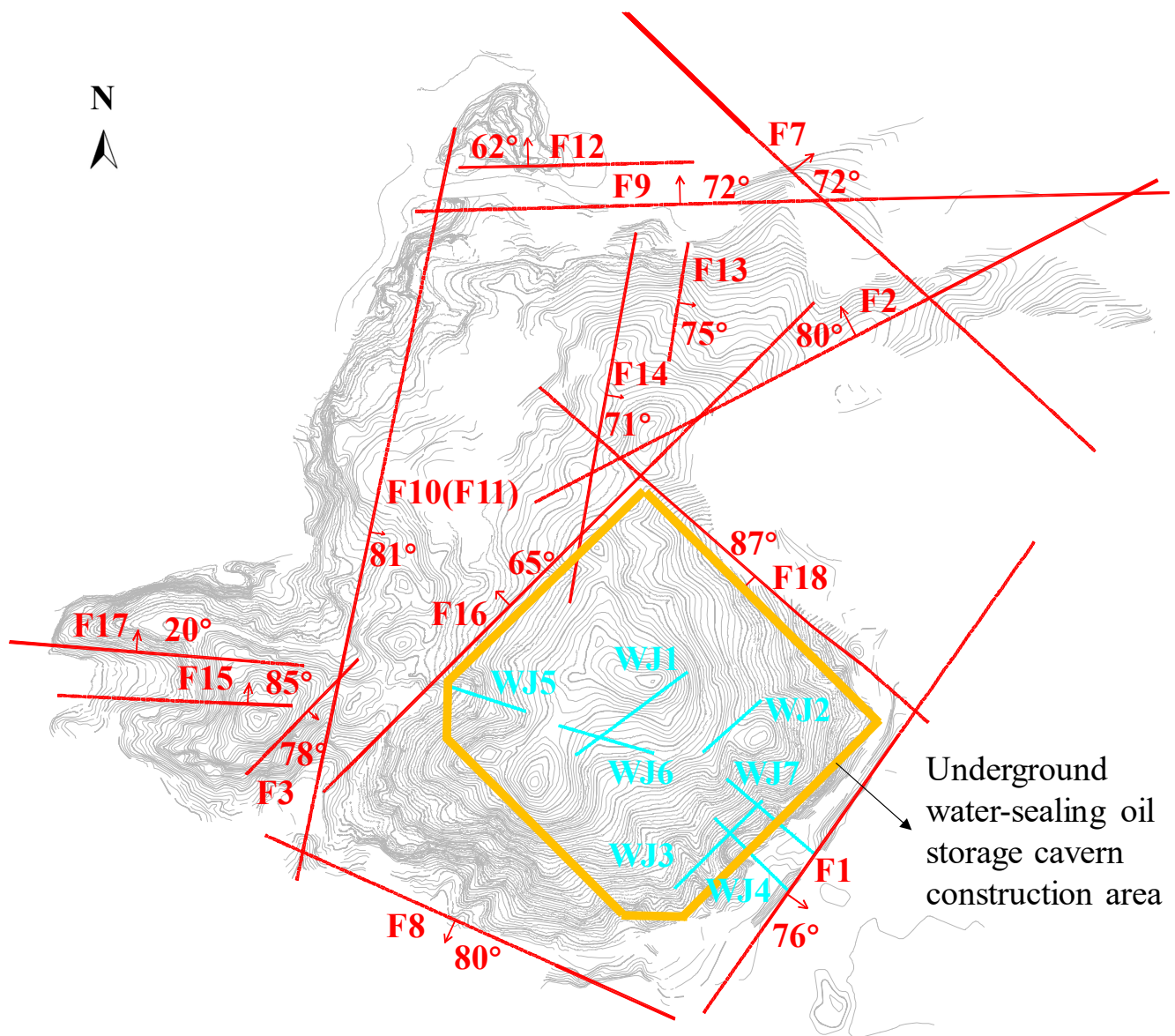

Figure 1. Faults and densely jointed zones in reservoir area.

2.3. Hydrogeology

The reservoir area connects to land on the south side and faces the sea on the east, north, and west sides, without obvious water system development around the reservoir area. The occurrence conditions of groundwater in the reservoir area are mainly fissured water in weathered or structural fissures of the bedrock, but the water volume is limited. Groundwater mainly receives vertical recharge from atmospheric precipitation. Groundwater discharge is mainly by evaporation and lateral runoff. According to the meteorological station data [32], the average annual precipitation in the region is between 977.5 mm and 1316.6 mm. The lowest and highest tide levels every 50 years are −3.96 m and +5.06 m, respectively.

3. Model Construction and Boundary Conditions

3.1. Hydrogeological Model

Based on the lithology, elevation, and geophysical exploration of 49 boreholes in the project feasibility stage, a refined three-dimensional hydrogeological model of the reservoir area is constructed using Midas GTS, as shown in Figure 2. The faults, fracture network, and hydrological and water level monitoring results are also incorporated into the model. The model domain is meshed by tetrahedral grids, with a total of 2,265,480 zones. Figure 3 shows the meshes of faults and densely jointed zones in the reservoir area. Figure 4 shows the layout of horizontal and vertical water curtain systems around the cavern. The spacings between the water injection holes of the system are 10 m. The elevation of the horizontal water curtain system is −37 m. The vertical water curtain system is 25 m above the main cavern and 30 m below the main cavern.
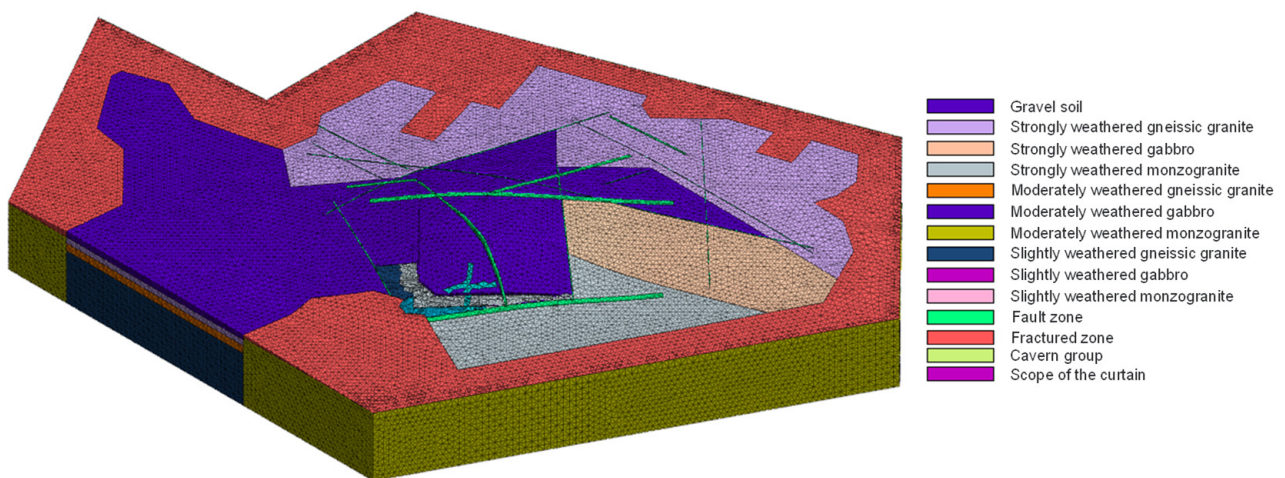

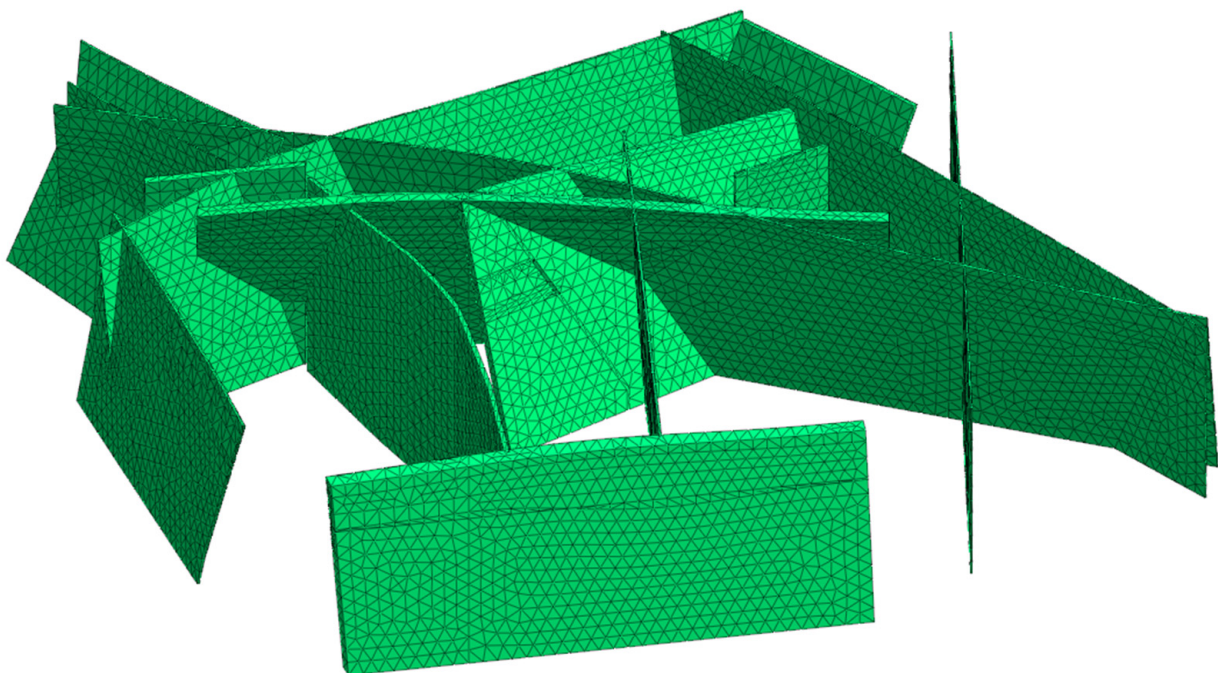**Figure 2.** Hydrogeological model of the reservoir area.

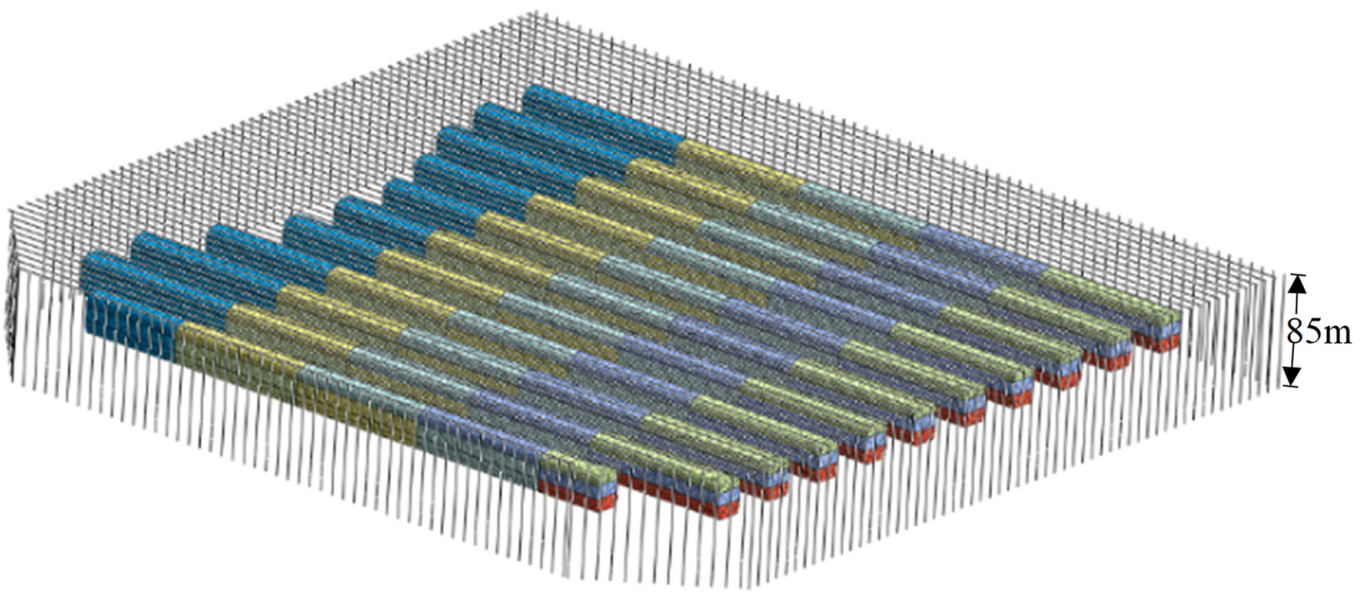**Figure 3.** Finite element mesh of faults and joint dense zones.

Figure 4. Schematic diagram of water curtain system around the cavern group.

3.2. Governing Equation

The research utilizes a finite-element software called PFST, which is developed by our team independently for numerical studies. The Galerkin finite element method, as well as Darcy's and Fick's laws, are used in the seawater intrusion program. The Picard method is used to deal with the nonlinear iteration issue, while the semi-implicit method is applied to the time problem. The convection–dispersion equation of seawater intrusion consists of two parts: the movement equation of groundwater flow and the solute transport equation. In the numerical simulation, the two equations are coupled by the multi-physical field coupling method. For porous rock and soil media, water flow can be described by the Darcy equation, which can be expressed as:

$$q_i = -k_\tau(p) K_{ij} \cdot \left(\frac{p}{\gamma} + z \right)_{,j} \tag{1}$$

where q_i is the Darcy velocity component in the i-th direction, $k_\tau(p)$ is the relative permeability coefficient ($0 \le k_\tau(p) \le 1$), K is the saturation permeability tensor of the medium, p is pore water pressure ($p > 0$ represents the medium is saturated, $0 \le p$ represents the medium is unsaturated), z is the elevation on the reference plane, and γ is unit weight.

According to the mass conservation principle, the saturated–unsaturated flow equation describing porous media can be derived, which can be expressed as:

$$\frac{\partial \theta}{\partial t} - \left[k_\tau(p) \cdot K_{ij} \cdot \left(\frac{p}{\gamma} + z \right)_{,j} \right]_{,i} = Q \tag{2}$$

where Q represents the source term, $i, j = 1, \ldots, D$ refers to the geometric coordinate subscript, $_{,i}$ represent the calculation of the partial derivative, and θ is the volumetric water content of the medium.

The basic equation of solute transport is:

$$\frac{\partial (\theta \cdot c)}{\partial t} - \left(\theta D_{ij} c_{,j} \right)_{,i} + (q_i c) - Q_s = 0 \tag{3}$$

where c is the concentration of a certain solute of the solution in soil pores, and Q_s is the pollution source. The expression of the dispersion coefficient D_{ij} is:

$$
\begin{aligned}
D_{xx} &= \alpha_L \frac{v_x^2}{|v|} + \alpha_{TH} \frac{v_y^2}{|v|} + \alpha_{TV} \frac{v_z^2}{|v|} + D^* \\
D_{yy} &= \alpha_L \frac{v_y^2}{|v|} + \alpha_{TH} \frac{v_x^2}{|v|} + \alpha_{TV} \frac{v_z^2}{|v|} + D^* \\
D_{zz} &= \alpha_L \frac{v_z^2}{|v|} + \alpha_{TH} \frac{v_x^2}{|v|} + \alpha_{TV} \frac{v_y^2}{|v|} + D^* \\
D_{xy} &= D_{yx} = (\alpha_L - \alpha_{TH}) \frac{v_x v_y}{|v|} \\
D_{xz} &= D_{zx} = (\alpha_L - \alpha_{TV}) \frac{v_x v_z}{|v|} \\
D_{yz} &= D_{zy} = (\alpha_L - \alpha_{TV}) \frac{v_y v_z}{|v|}
\end{aligned}
\tag{4}
$$

where v is the velocity of the fluid in the pore, α_L is the longitudinal dispersion coefficient, α_{TH} is the horizontal transverse dispersion coefficient, α_{TV} is the vertical transverse dispersion coefficient, and D^* is the effective molecular diffusion coefficient of the solute.

3.3. Boundary Conditions

In the finite element code, the coupling of the seepage field and solute transport field is realized by integrating multiple physical fields. The seepage field satisfies Darcy's law, and the solute transport field mainly depends on solute convection–dispersion rules. The seawater intrusion model hereby incorporates both the Darcy seepage field and the solute transport field. The model includes an inland boundary, a three-side seawater boundary, a top boundary, a bottom boundary, a cavern boundary, a water curtain boundary, etc. For the boundary conditions, the southern inland boundary is treated to be impervious. The top boundary is set as a flow boundary considering rainfall infiltration and evaporation. According to the annual precipitation data from meteorological stations, the average precipitation of the top inland boundary is about 1000 mm, and the specific flow value of the top boundary is determined by combining it with the water level measurements of drilled boreholes. The impervious bottom boundary is set at an altitude of −400 m. The seawater boundaries on the east, west, and north sides are set 150 m–250 m away from the continental shelf, as shown in Figure 5. The water head boundary is set at the top of the continental shelf, and the water head value is obtained based on the seawater level (the lowest tide level is −3.96 m per 50 years, and the highest tide level is +5.06 m per 50 pears). In the calculation of the seepage field during cavern excavation and operation, the boundary of the cavern is set as a possible overflow surface, and the overflow water level is −100 m. The boundary of the water curtain hole is determined by the iterative method.

The Cl^- is selected as the representative ion for solute transport field calculation. The risk of seawater intrusion is analyzed by estimating the change in Cl^- concentration. The Cl^- concentrations in the seawater, groundwater, and freshwater of the model are 500 mol/m³, 3 mol/m³, and 0.0014 mol/m³, respectively. During the actual operation, the water in the water curtain hole exchanges with the groundwater of the surrounding rock mass, making it difficult to maintain the initial concentration value of Cl^- in the water curtain hole. As a result, two Cl^- concentration levels in water curtain holes are considered in modeling: 3 mol/m³ and 0.0014 mol/m³.
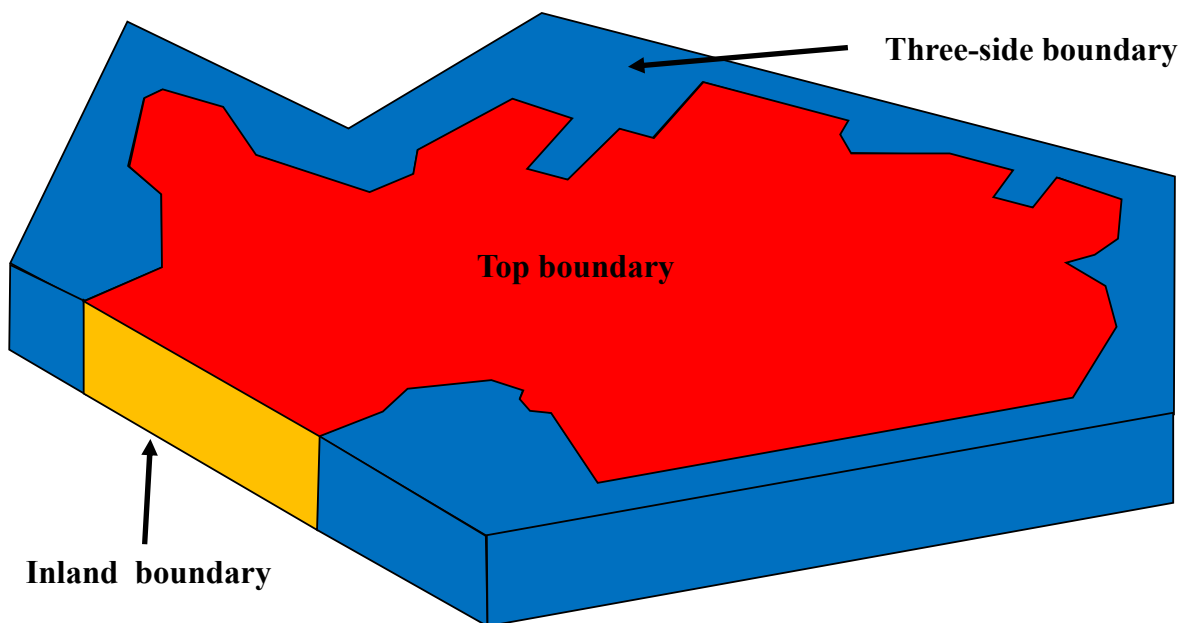
Figure 5. Partial boundaries of the model.

3.4. Material Parameters

The model includes 17 material types, such as gravel soil, gneiss granite, gabbro, monzonite, silt, etc. According to pressurized water testing, the permeability coefficient in the field ranges between 2.54×10^{-11} m/s and 3.24×10^{-6} m/s. On the east boundary, a high permeability coefficient is found between 1.0×10^{-8} m/s and 7.0×10^{-7} m/s. The permeability coefficient around the cavern ranges from 5.0×10^{-9} m/s to 3.0×10^{-7} m/s. The seepage parameters of each material are shown in Table 1. The specific yield is determined by engineering experience, and it is between 0.1 and 0.15 for the quaternary loose sediment and the fully weathered section. The small faulting zone and the moderately weathered zone have a specific yield between 0.05 and 0.1, and the specific yield of slightly weathered rock mass is between 0.005 and 0.05. The unit storage capacity is determined according to the literature [33]. The values of rock mass dispersion and molecular diffusion coefficient [34] are shown in Table 2. Freshwater and seawater densities are 1000 kg/m^3 and 1030 kg/m^3, respectively.

Table 1. Material parameters for seepage field calculation.

Type of Rock Mass	Permeability Coefficient (m/s)	Specific Yield	Unit Storage Capacity (1/m)
Fault zone	8.00×10^{-7}	0.1	2×10^{-6}
Densely jointed zone	1.00×10^{-7}	0.1	2×10^{-6}
Gravel soil	8.00×10^{-7}	0.15	2×10^{-6}
Strongly weathered monzogranite	8.00×10^{-7}	0.1	2×10^{-6}
Strongly weathered gabbro	8.00×10^{-7}	0.1	2×10^{-6}
Strongly weathered gneissic granite	8.00×10^{-7}	0.1	2×10^{-6}
Moderately weathered gabbro	3.08×10^{-7}	0.02	1×10^{-6}

Table 1. *Cont.*

Type of Rock Mass	Permeability Coefficient (m/s)	Specific Yield	Unit Storage Capacity (1/m)
Moderately weathered monzogranite	3.01×10^{-7}	0.02	1×10^{-6}
Moderately weathered gneiss granite	4.52×10^{-7}	0.02	1×10^{-6}
Slightly weathered gabbro	8.21×10^{-9}	0.002	1×10^{-7}
Slightly weathered monzogranite	2.46×10^{-8}	0.002	1×10^{-7}
Slightly weathered gneissic granite	1.27×10^{-8}	0.002	1×10^{-7}
Water curtain section (elevation between −30 and −37 m)	4.00×10^{-8}	0.002	1×10^{-7}
Cavern section (elevation between −62 and 92 m)	1.00×10^{-8}	0.002	1×10^{-7}
Between bottom of water curtain and top of cavern (elevation between −37 and −62 m)	2.00×10^{-8}	0.002	1×10^{-7}
silt	3.89×10^{-7}	0.0001	1×10^{-8}
Continental shelf	1.00×10^{-8}	0.05	1×10^{-7}
Fractured zone	3.89×10^{-7}	0.1	2×10^{-6}

Table 2. Solute transport parameters.

Type of Rock Mass	Longitudinal Dispersion Coefficient (m)	Transverse Dispersion Coefficient (m)	Molecular Diffusion Coefficient (m^2/s)
Fault zone and strongly weathered rock mass	2	0.5	2×10^{-7}
Moderately and slightly weathered rock mass	1	0.1	2×10^{-8}

4. Results and Discussion

4.1. Seepage Field and Seawater Intrusion in Natural State of Reservoir Site

4.1.1. Natural Seepage Field in Reservoir Area

The groundwater level is measured through 60 drill holes on site, and its contour map is obtained by the Kriging interpolation method, as shown in Figure 6. The water level in the northwest of the cavern is much higher than that on other sides, while the water level in the southeast is the lowest. A reasonable value of permeability coefficient in cavern area is very important for the estimation of water inflow, supply water quantity of water curtain system, and seawater intrusion. Therefore, the model is divided with different permeability coefficients according to the actual condition. The modeled seepage field under the natural state is obtained inversely by modifying the permeability coefficient of the outer cavern. The permeability coefficients at elevations from −38 to −20 m, from −62 m to −38 m, and from −92 m to −62 are shown in Figure 7a–c, respectively. The cavern and its vicinity are divided into 12 zones with various permeability coefficients, as shown in Table 3. Inputting the permeability coefficients, the simulated water levels in Figure 8 are basically consistent with the field water level measurements in Figure 6.

4.1.2. Seawater Intrusion Situation in The Reservoir Area before Construction

The solute transport is analyzed to reflect the seawater intrusion situation in the natural state before construction. By taking the natural seepage field as the initial model condition, the unbalanced solute transport is calculated until the solute transport field is converged. Because the groundwater level corresponding to the high tide condition leads to higher seawater intrusion risks, the seawater boundary is treated according to the high tide level in the modeling. A sectional view of Cl$^-$ concentration contour crossing the middle cavern is illustrated in Figure 9. According to the Chinese standard DD2008-03, 7 mol/m^3 Cl$^-$ is the threshold between saltwater and freshwater, which is thus regarded as the seawater intrusion boundary in this investigation. As the result shows that the Cl$^-$ concentration around the cavern is less than 7 mol/m^3, the oil storage cavern has no seawater intrusion risks in the natural state.
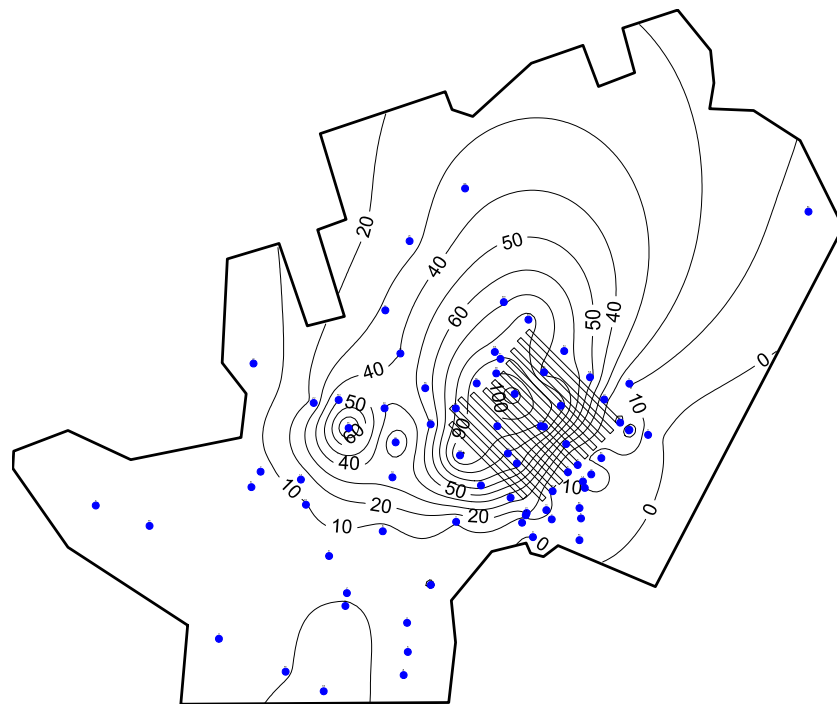
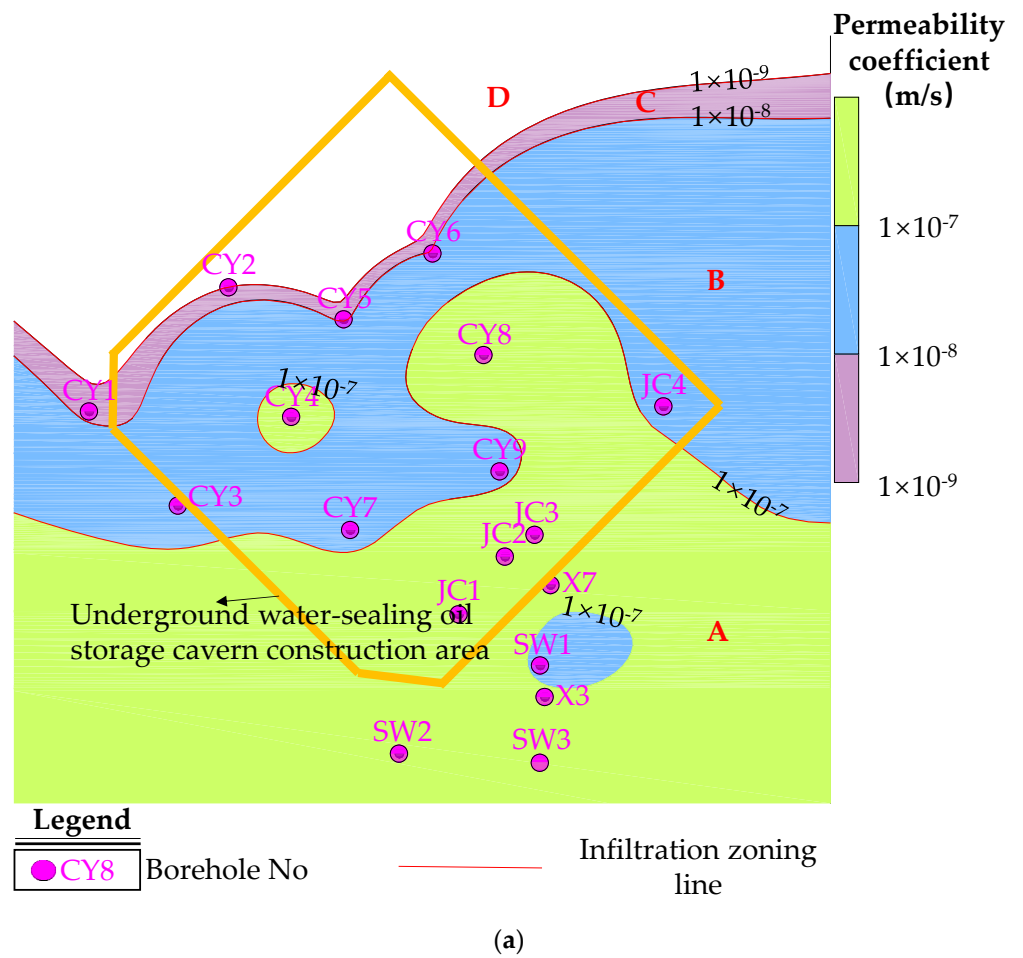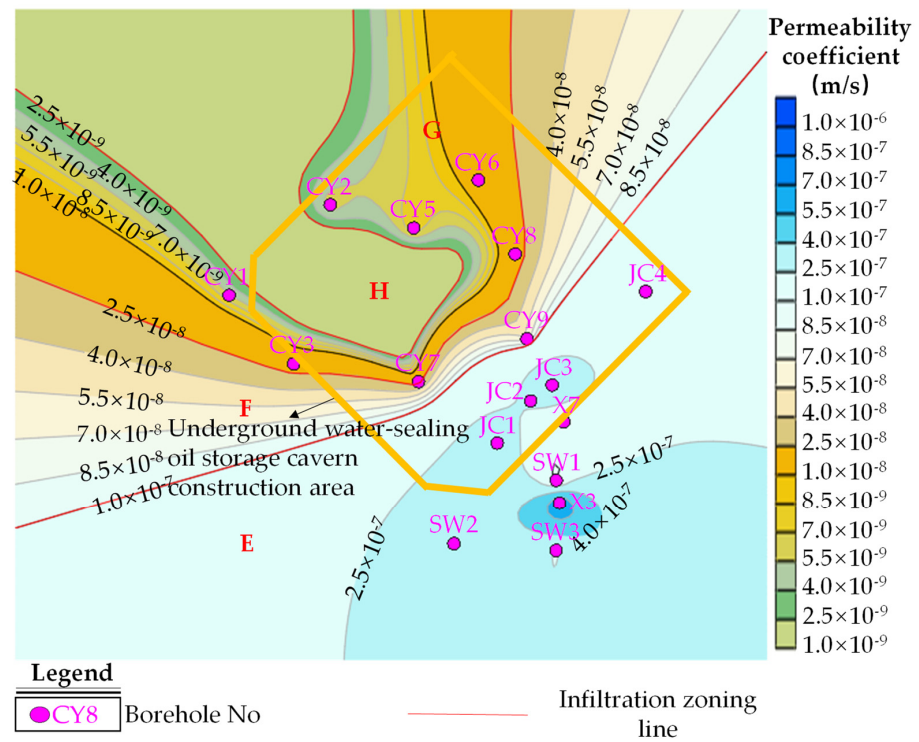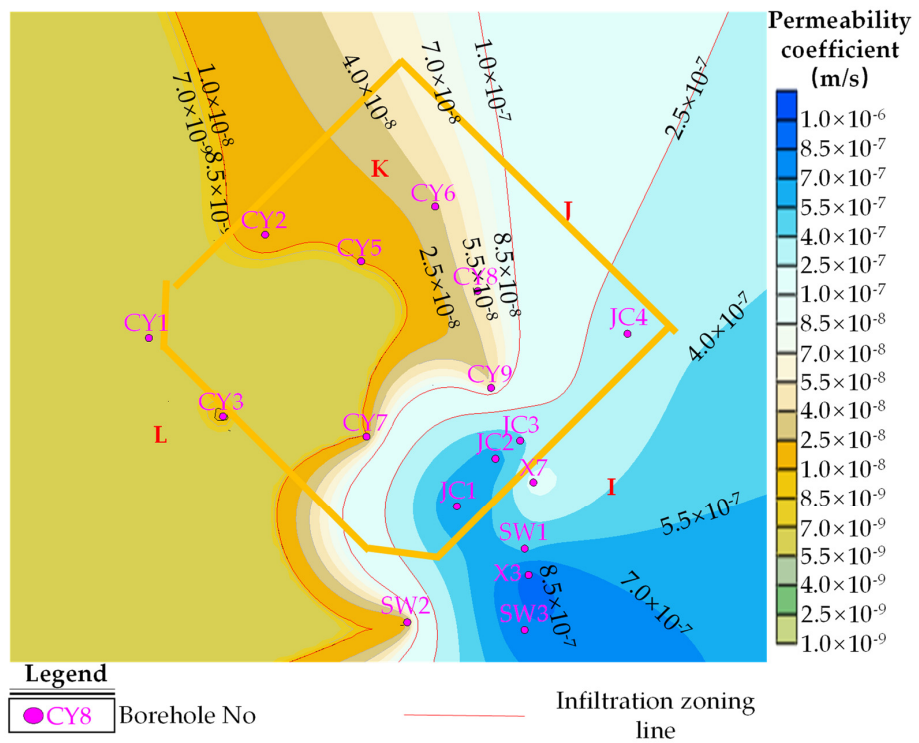**Figure 6.** Water level contour measured from boreholes (blue dots).

(**a**)

Figure 7. *Cont.*

(**b**)

(**c**)

Figure 7. Permeability coefficient distribution at different elevations in the model: (**a**) between −38 and −20 m; (**b**) between −62 and −38 m; (**c**) between −92 and −62 m.

Table 3. Permeability coefficients corresponding to each zone of cavern.

Partition	Zone	Permeability Coefficient (m/s)
Elevation between −38 and −20 m (water curtain section)	A	4×10^{-7}
	B	5×10^{-8}
	C	5×10^{-9}
	D	1×10^{-9}
Elevation between −62 and −38 m (between water curtain and cavern top)	E	3×10^{-7}
	F	3×10^{-8}
	G	6×10^{-9}
	H	1×10^{-9}
Elevation between −92 and −62 m (cavern section)	I	6×10^{-7}
	J	2×10^{-7}
	K	5×10^{-8}
	L	7×10^{-9}
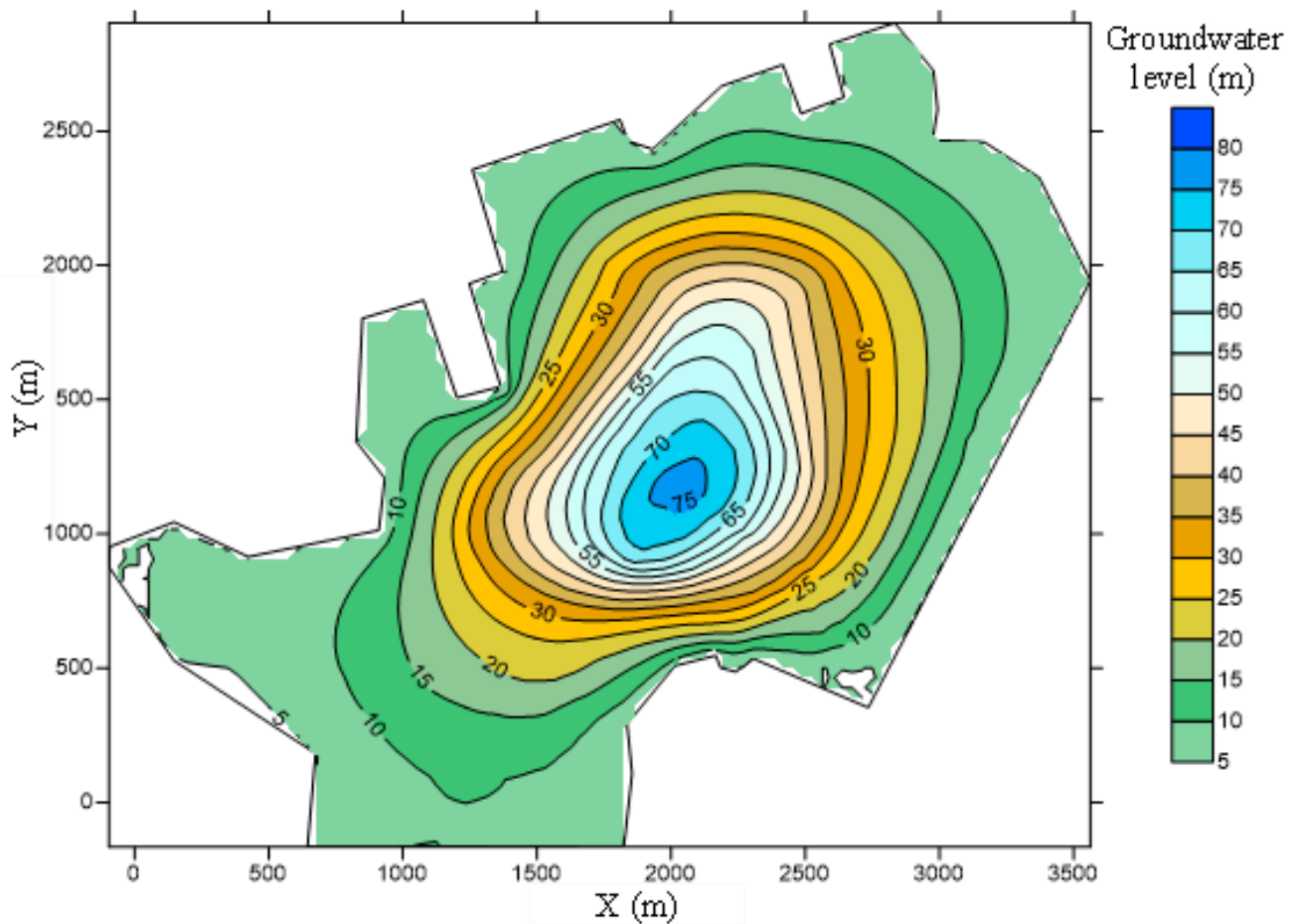
Figure 8. Isolines of modeled natural groundwater level in the reservoir area under high tide conditions.
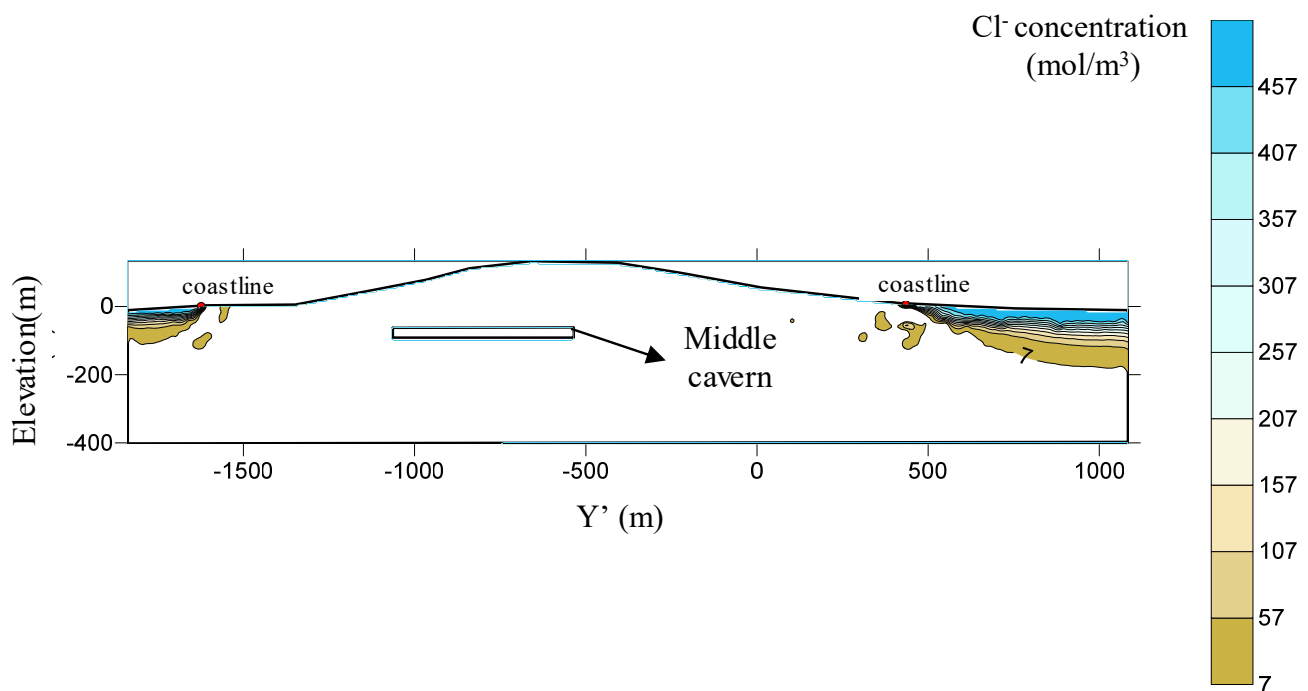
Figure 9. A sectional view of Cl$^-$ concentration contour crossing the middle cavern.

4.2. Unsteady Seepage Field and Seawater Intrusion Risk during the Cavern Construction

4.2.1. Unsteady Seepage Field

During cavern excavation, both grouting and water curtain systems are applied. The supplementing water pressure from water curtain holes is 0.47 MPa. Under the designed high tide condition, the groundwater level contour at the end of the excavation is shown in Figure 10. Compared with the natural condition, the groundwater level in the reservoir area decreases significantly, but not the case in the vicinity of the cavern. The cavern construction reduces the water head around the cavern, weakening the convection of freshwater to seawater and increasing the risk of seawater intrusion. Figure 11 shows the contour and gradient vector map of the water head in Section 2 (see Figure 12) after cavern excavation. As can be seen from Figure 11a, the water head in the reservoir area decreased significantly due to the excavation. The water head value on the southeast side is smaller than that in other areas, but it is still higher than the seawater level. Additionally, Figure 11b reveals the flow direction on the southeast side is from inland to the sea, meaning low seawater intrusion risk.

Figure 13 shows the variation in cavern water inflow and water supply volumes from the water curtain system during the excavation of the main cavern. After excavating the top, middle, and bottom layers of the main cavern, the water inflows are 6797 m^3/day, 6895 m^3/day, and 6767 m^3/day, respectively. During the same period, the supplied water quantity from the water curtain system is lower than the cavern inflow, with a maximum water supply of 6039 m^3/day. Two curves in Figure 13 demonstrate consistent changes with time. They increase rapidly when the top of the cavern is excavated before turning stable when the middle and bottom of the cavern are excavated. From Day 150 to Day 240, the water inflow of the cavern increases greatly due to a higher permeability coefficient on the southeast side of the cavern than on the northwest side. After the excavation, the water inflow in the cavern before oil storage is 6690 m^3/day, and the supplied water quantity from the curtain system is 6061 m^3/day.
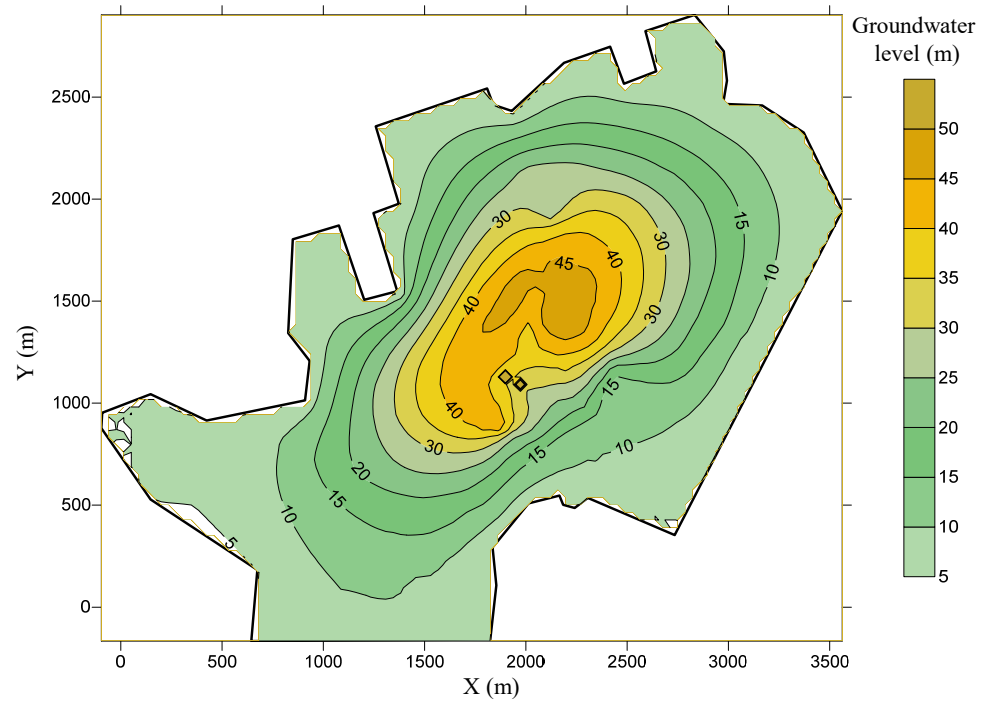
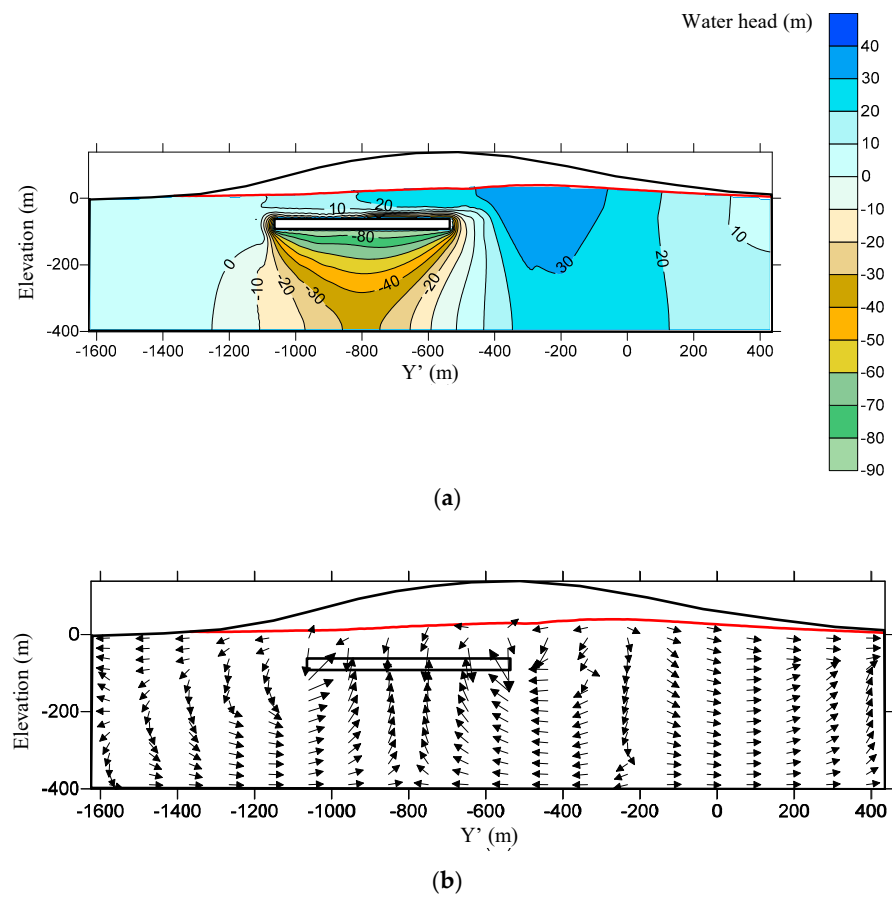**Figure 10.** Groundwater level after cavern bottom excavation.

(**a**)

(**b**)

Figure 11. Water head condition after cavern bottom excavation: (**a**) water head contour; (**b**) water head gradient vector diagram.
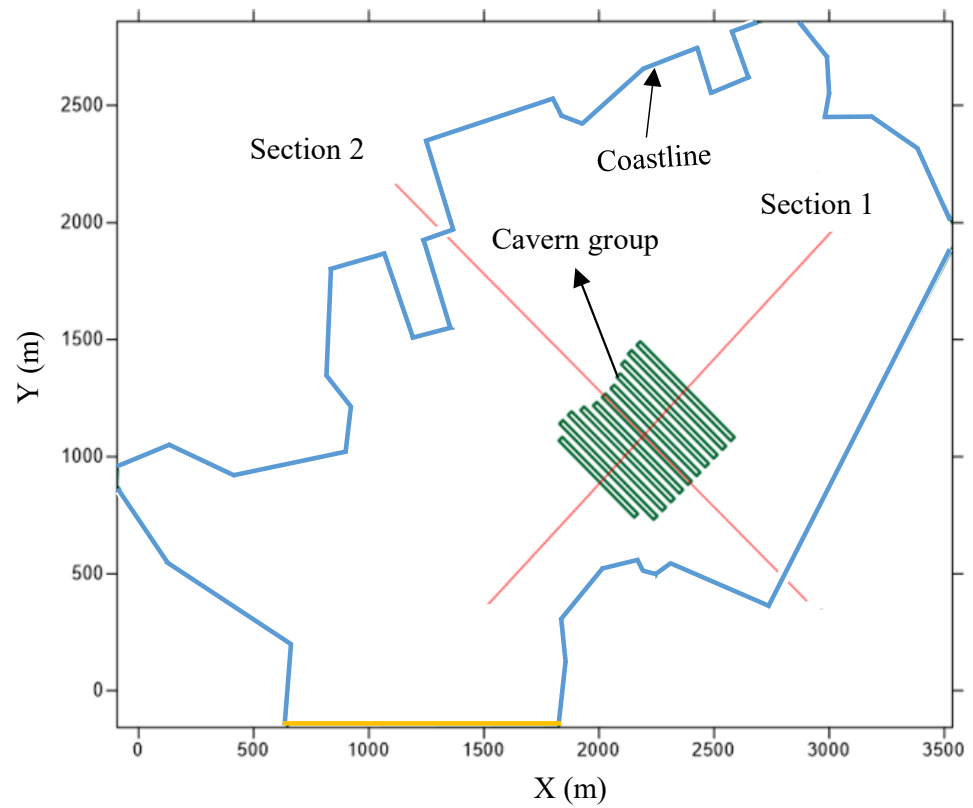
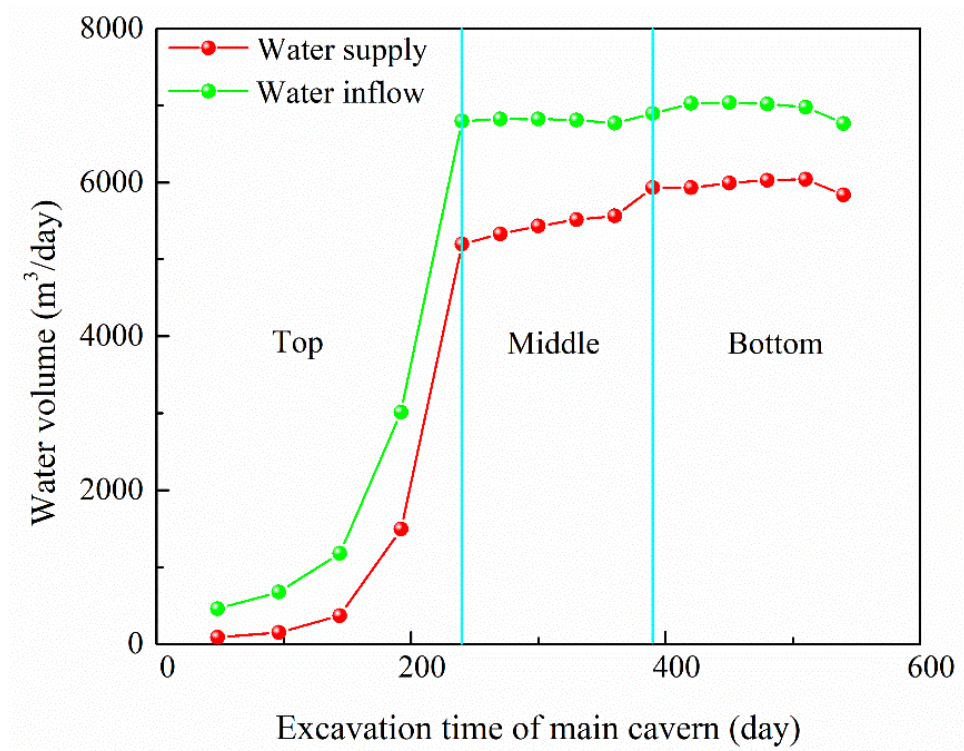**Figure 12.** Section positions on plane view.

Figure 13. Changes in water inflow and water supply of water curtain system during the excavation of the main cavern.

4.2.2. Seawater Intrusion Risk during Construction

During the cavern excavation and drainage process, the water pressure around the cavern falls accordingly, increasing the possibility of seawater invasion. Under the high tide water level condition, the Cl$^-$ concentration contour on Section 2 after cavern construction is shown in Figure 14. The Cl$^-$ concentration of the cavern area is less than 7 mol/m^3, showing minimal seawater intrusion risk during the excavation period. The Cl$^-$ concentration at -80 m elevation on a plane view cutting the cavern group is shown in Figure 15. It shows Cl$^-$ concentration is greater than 7 mol/m^3 around the southeast corner of the cavern. This could be attributed to the broken rock mass structure in the southeast area of the reservoir with the presence of faults and densely jointed zones. The corresponding permeability coefficients in this area are up to 6×10^{-7} m/s, showing strong water conductivity.
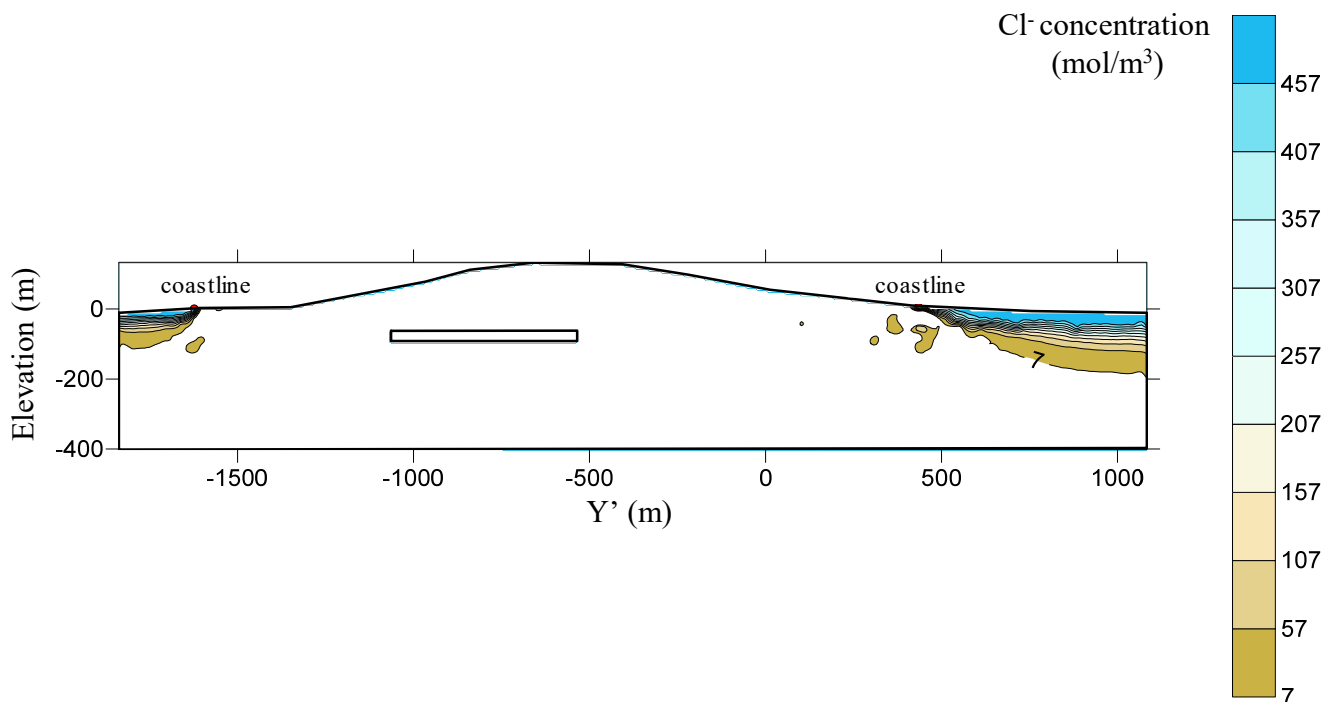
Figure 14. Cl$^-$ concentration contour map of Section 2 at the end of cavern construction.

The dispersion of seawater to freshwater will be enhanced with the groundwater level drop due to excavation. Consequently, the analysis and monitoring of seawater intrusion should focus on the southeast area during the long-term operation of the underground oil storage cavern.

4.3. Seawater Intrusion Risk and Control during the Cavern Operation

4.3.1. Seepage Field and Seawater Intrusion Risk with Horizontal Water Curtain System

(1)   Steady seepage field during operation

The water pressure of the water curtain holes is set as 47 m water head in the calculation model. The cavern boundary is treated as the known pressure boundary in the case of oil storage in the cavern. The absolute pressure in the main cavern during the operation period is 0.12 ~ 0.28 MPa. Considering that the oil density is about 900 kg/m^3, a 20 m water head is applied to the cavern's inner boundary. Figure 16 shows the water head contours at the top and bottom of the cavern group, respectively. The water head changes differently around the reservoir area. The water head value is relatively higher on the northwest side affected by fault F14 and higher on the southeast side due to F1 and F8 faults and densely jointed zones close to the sea.
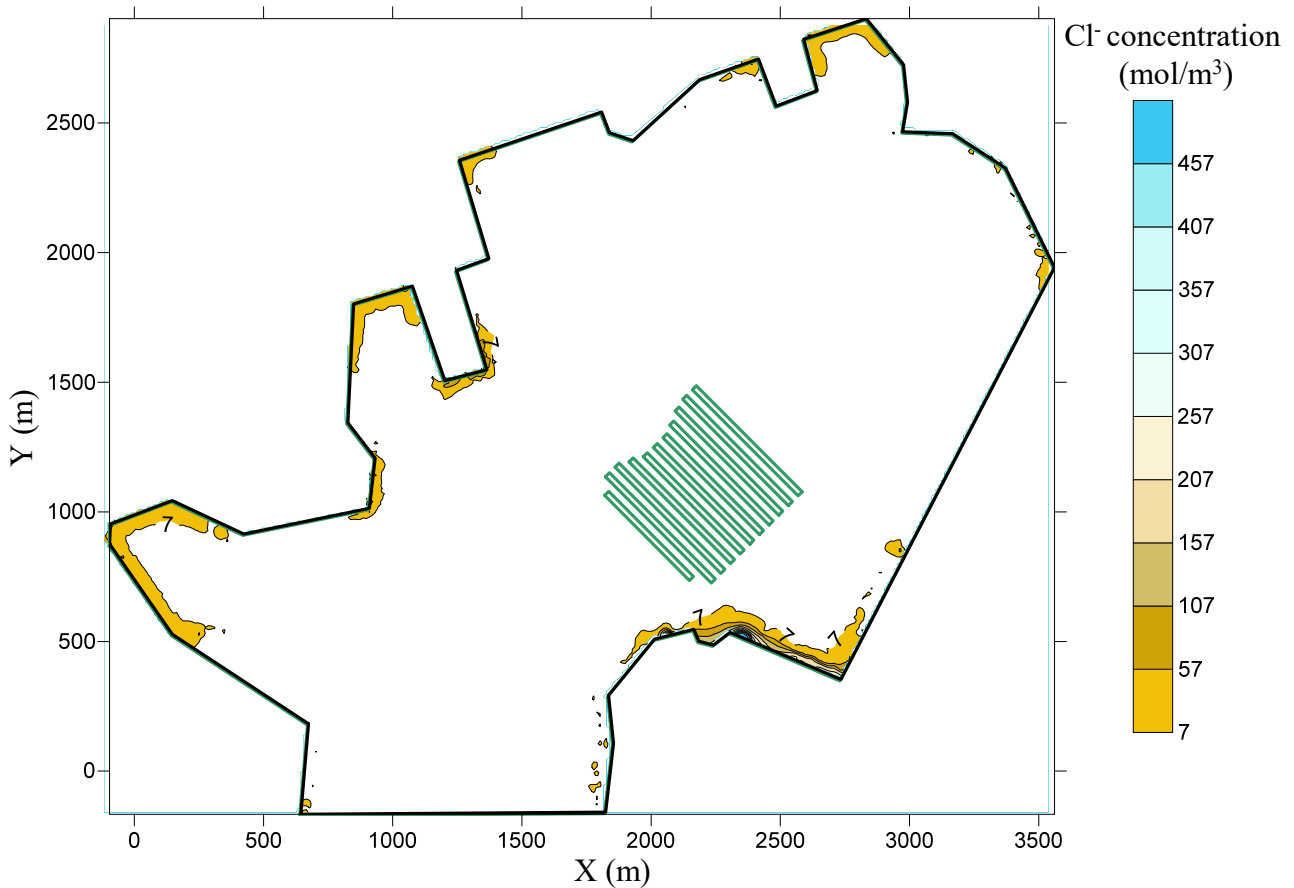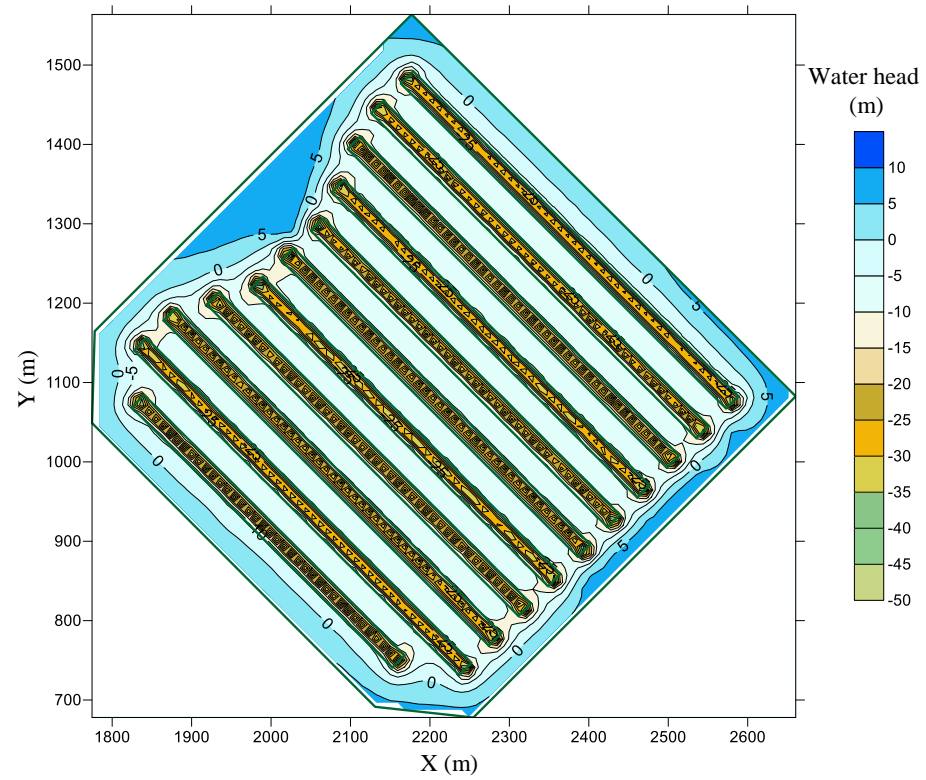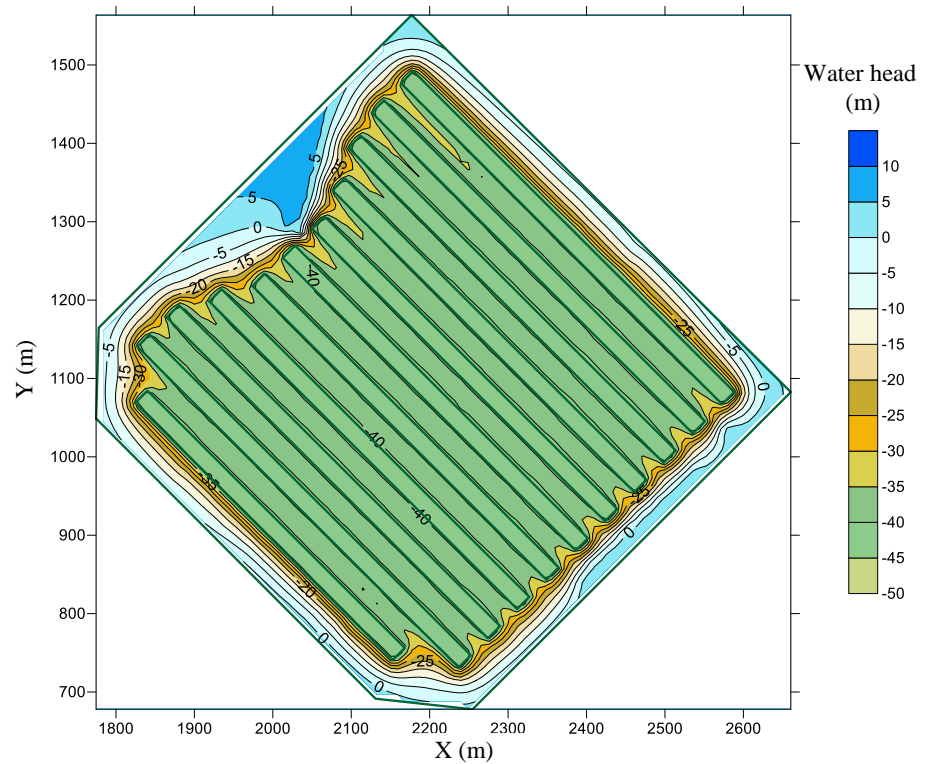
Figure 15. Cl⁻ concentration contour at −80 m elevation at the end of construction.

(2) Seawater intrusion risk

Figure 17 depicts the Cl⁻ concentration contour at −80 m elevation in the reservoir region after 50 years of cavern operation using the horizontal water curtain system, with the groundwater injected into the water curtain hole. It can be observed that the Cl⁻ concentration on the southeast side exceeds 7 mol/m³, which means seawater has invaded the southeast side of the cavern group. Figure 18 illustrates the Cl⁻ concentration at the cavern bottom (−92 m elevation) after 50 years of operation with groundwater or freshwater injected into curtain holes. It is seen that the migration of Cl⁻ in groundwater is not uniformly diffused and is affected by geology, rock weathering, and other factors. In addition, the Cl⁻ concentration on the southeast side of the cavern group exceeds 50 mol/m³, suggesting the highest risk of seawater intrusion. This might be caused by the seawater intrusion along the fault zone and the densely jointed zone with high permeability. The northwest and northeast sides have no seawater intrusion risk. According to the Chinese standard GB50021-2009, the groundwater corrosion rating on the southeast side could reach moderate corrosion (Table 4). The main reason for the seawater intrusion could be the excavation-induced groundwater level drop, which decreases freshwater hydraulic gradient and weakens freshwater convection to seawater, so the diffusion between seawater and freshwater is gradually strengthened. Figure 17 demonstrates that the seawater intrusion risk at the bottom of the cavern is much greater than at the top. Because seawater has a higher density than freshwater, it will infiltrate the cavern from the bottom. Figure 19 depicts the change in Cl⁻ concentration on the southeast side of the bottom of Cavern #2 over time. After 18 years of operation, the cavern is at risk of saltwater intrusion when just the horizontal water curtain is used, regardless of whether groundwater or freshwater is injected into the water curtain.

(**a**)

(**b**)

Figure 16. Water head contours when setting horizontal water curtain system: (**a**) at the cavern top (−62 m elevation); (**b**) at the cavern bottom (−92 m elevation).
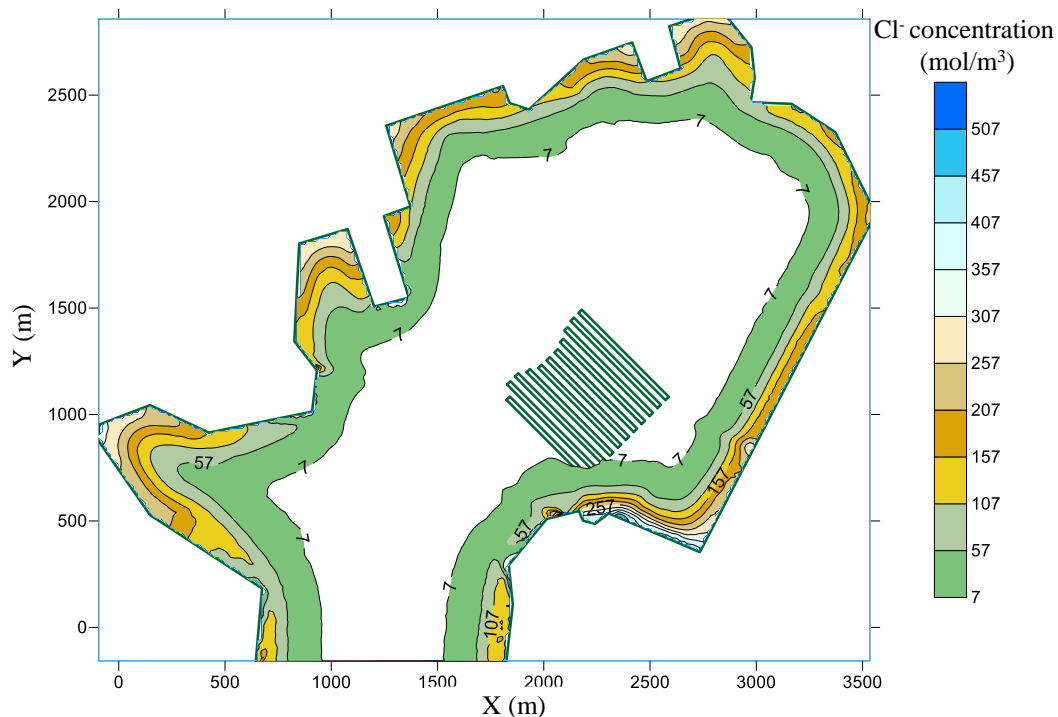
Figure 17. Cl⁻ concentration contour at −80 m elevation with groundwater injection in the curtain system after 50 years operation.

4.3.2. Seepage Field and Seawater Intrusion Risk with Horizontal and Vertical Water Curtain Systems

The above analysis shows that the seawater intrusion risk at the bottom of the cavern is the highest; thus, the bottom seepage and solute transport fields need to be focused on. Figure 20 shows the water head contour at the cavern bottom when horizontal and vertical water curtain systems are applied. Compared to the results without the vertical water curtain system in Figure 16, the water head in the southeast of the cavern group rises obviously. This finding is consistent with the conclusion of Wang et al. [26] that the water curtain system plays an essential role in water replenishment for groundwater level lift.

Figure 21 shows the Cl⁻ concentration at the cavern bottom after 50 years of operation. The Cl⁻ concentration is significantly lower than when only using a horizontal water curtain system. This conclusion is in line with the results of Li et al. [25] that the water curtain system can effectively inhibit seawater intrusion. When injecting groundwater in the water curtain system, the Cl⁻ concentration on the southeast side of the cavern decreases from 52.3 mol/m³ to 5.1 mol/m³ in Figure 21a, and it drops further to 3.01 mol/m³ if freshwater is injected in the system in Figure 21b. Regardless of using groundwater or freshwater, the Cl⁻ concentration around the cavern is less than 7 mol/m³ during 50 years of operation. This shows that the addition of a vertical water curtain increases the water level of freshwater near the reservoir area, effectively inhibiting seawater intrusion. Figure 22 shows the Cl⁻ concentration on the bottom of Cavern #2 during the operation period. The groundwater is injected into the water curtain holes, and the Cl⁻ concentration in the cavern increases gradually over time, especially in the southeast of the reservoir area.
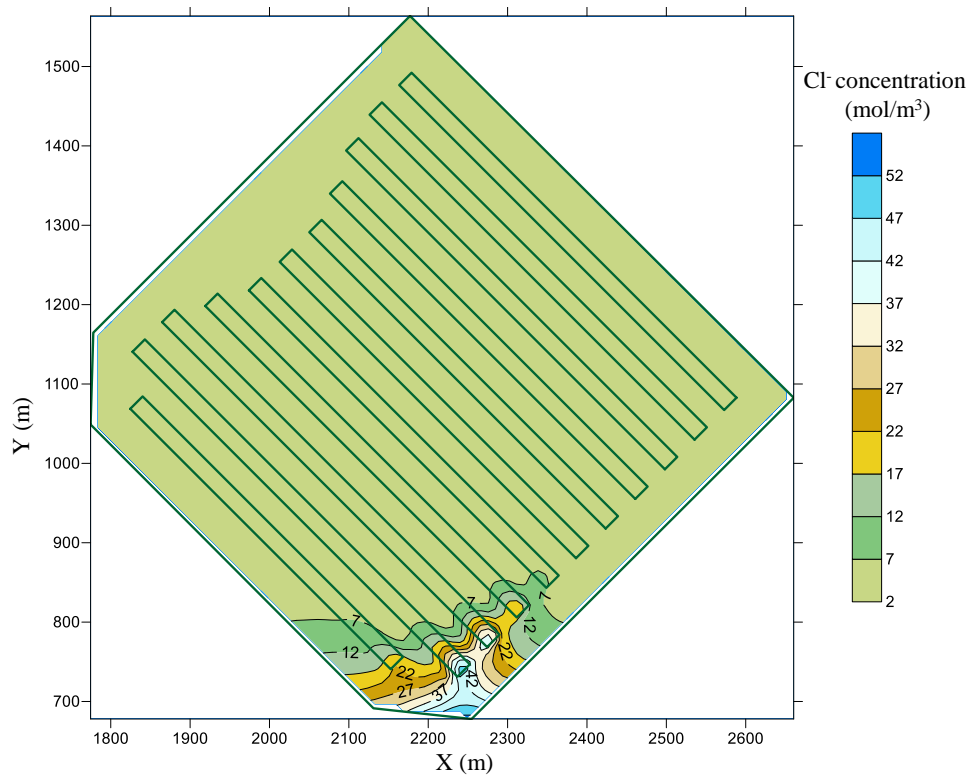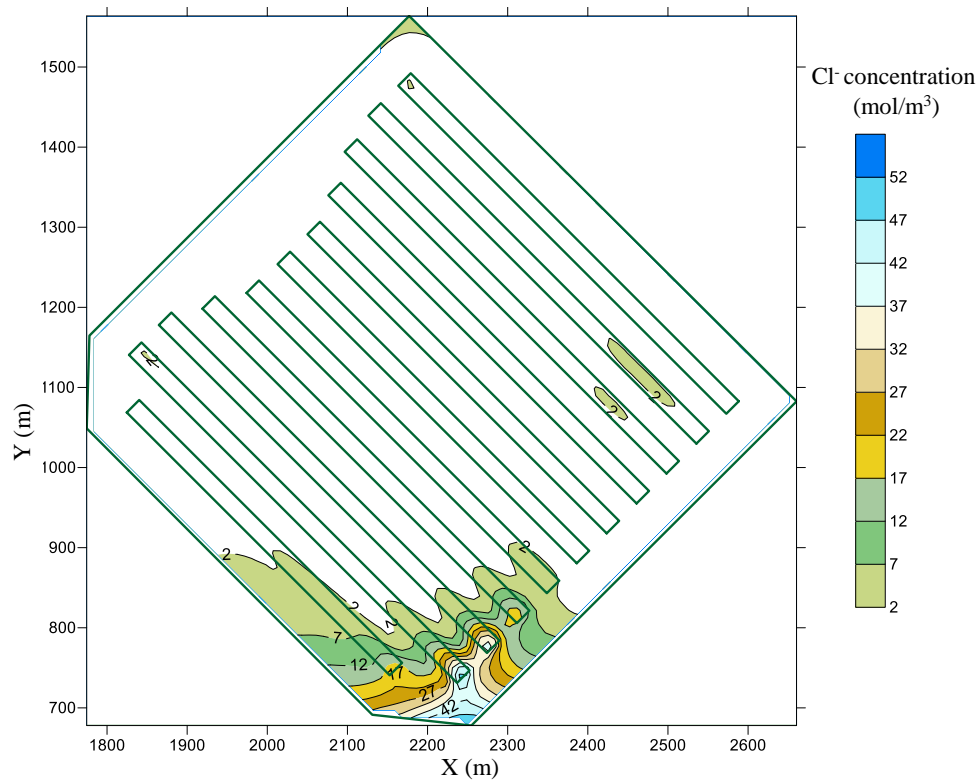
Figure 18. Cl⁻ concentration at the cavern bottom (−92 m elevation) after 50 years operation: (**a**) groundwater injection in water curtain system; (**b**) freshwater injection in water curtain system.

Table 4. Reinforcement steel corrosion rating.

| Corrosion Rank	Micro Corrosion	Slight Corrosion	Moderate Corrosion	Strong Corrosion
Cl^- concentration (mol/m^3)	<3	3 ~ 14.3	14.3 ~ 143	>143
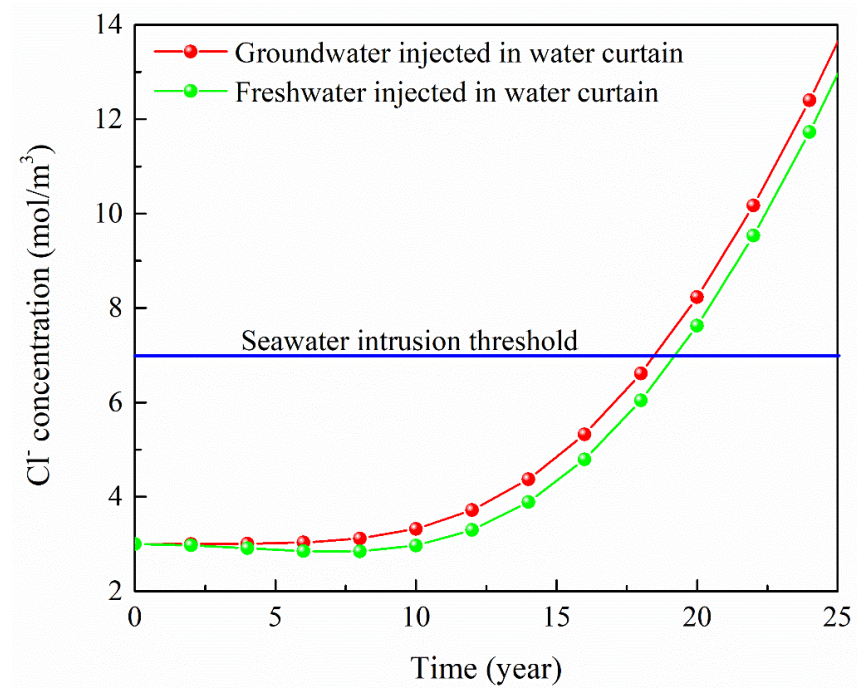
Figure 19. Cl^- concentration on the southeast side of the bottom of Cavern #2 with time.
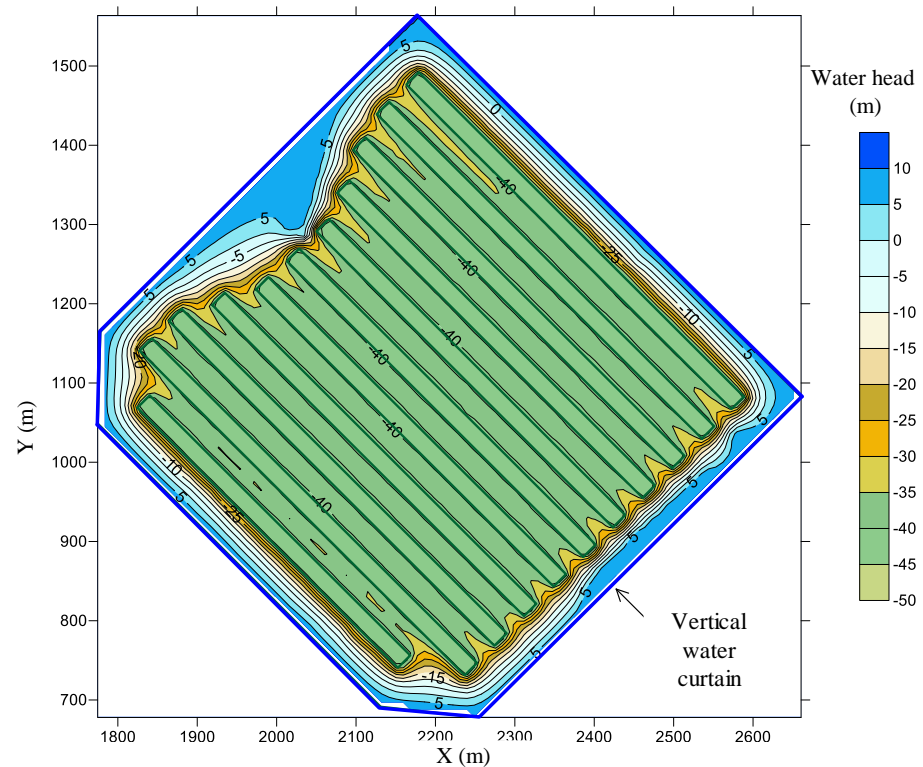
Figure 20. Water head contour at the cavern bottom after 50 years of operation.
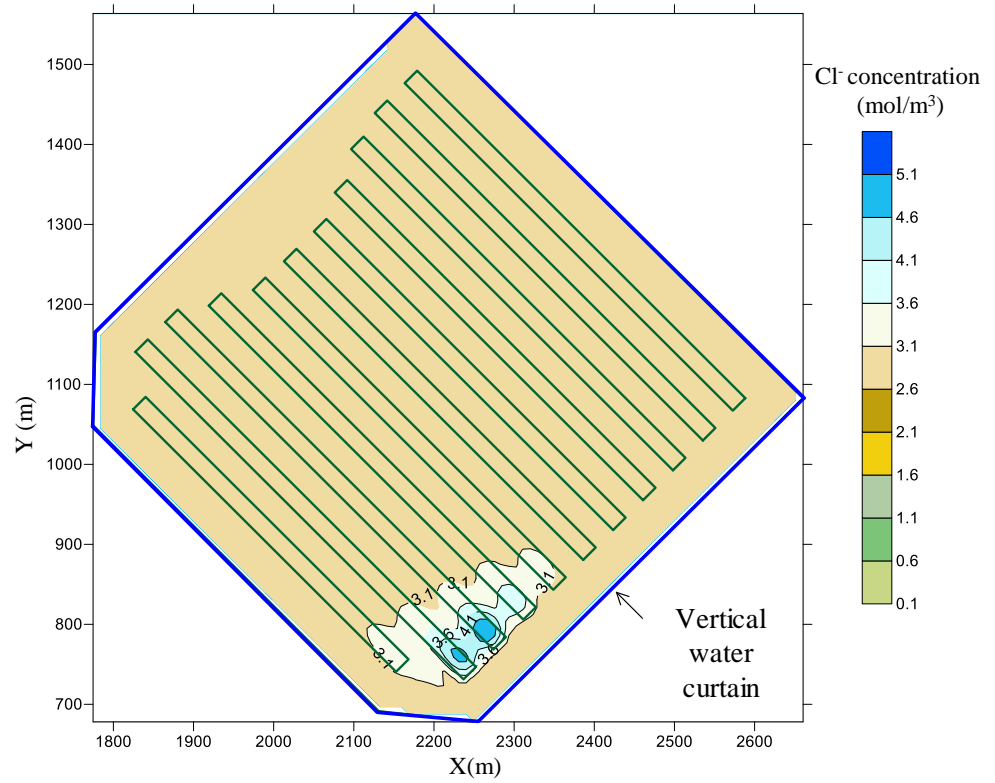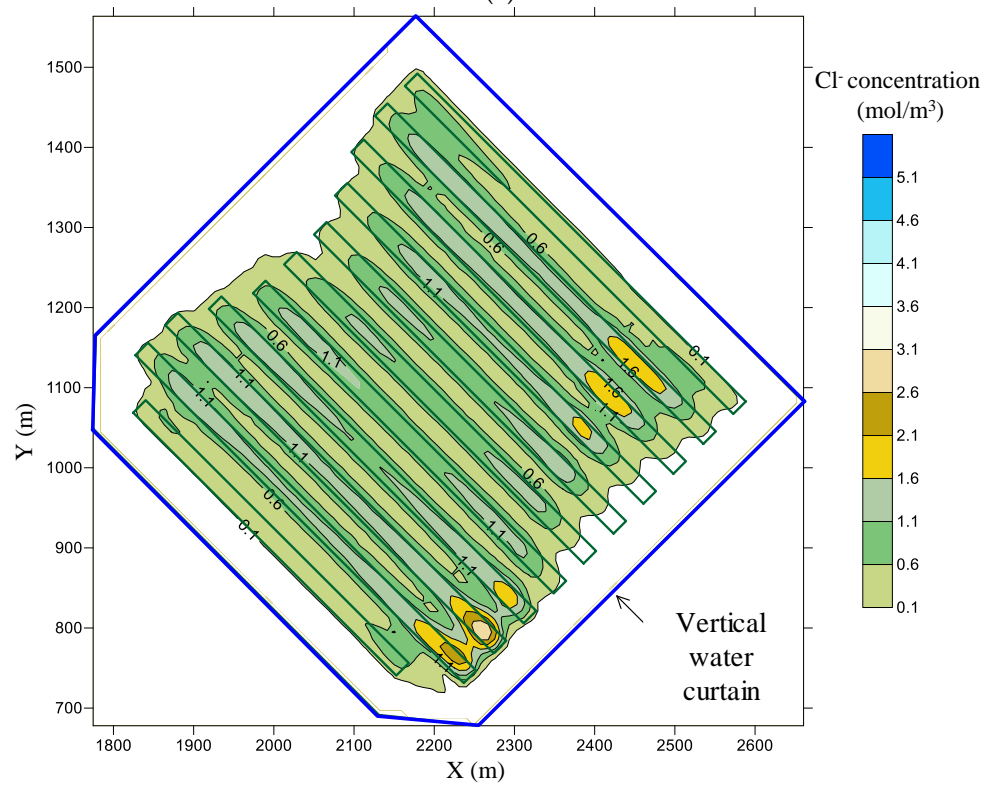
Figure 21. Cl⁻ concentration on the bottom of the cavern after 50 years of operation: (**a**) groundwater injected into the water curtain system; (**b**) freshwater injected into the water curtain system.
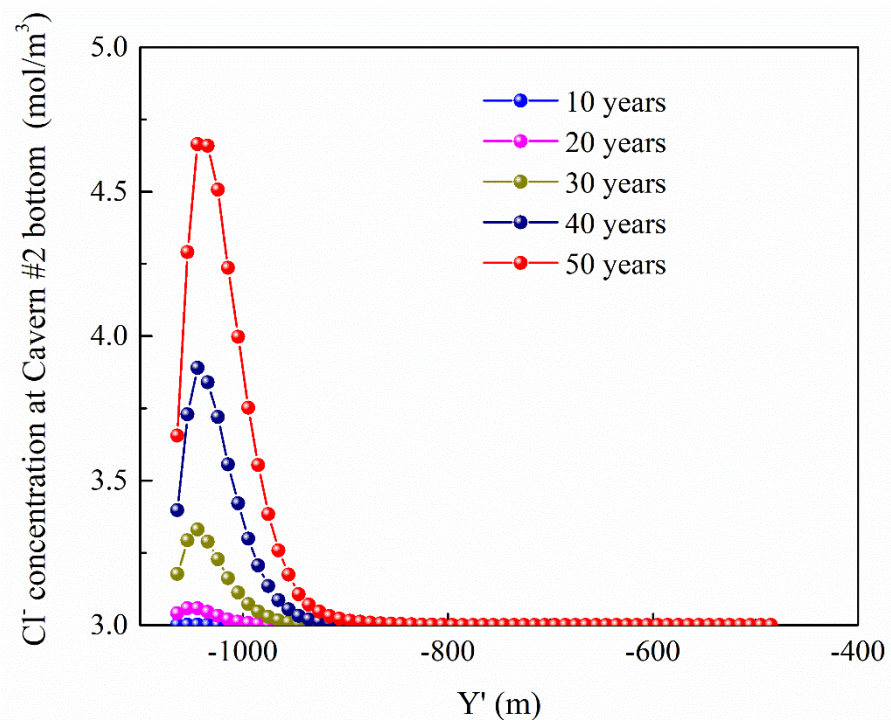
Figure 22. Cl^- concentration on the bottom of Cavern #2 during the operation period.

The southeast side of the cavern group is the riskiest area for seawater intrusion. By considering the construction and operation cost of the water curtain, the seawater intrusion risk is analyzed when a vertical water curtain system extending to 30 m below the cavern with 10 m hole spacing is only applied in the southeast of the cavern group. The distribution of Cl^- concentration at the cavern bottom after 50 years of operation is shown in Figure 23. Compared with the vertical water curtain system surrounding the whole cavern group, the maximum value of Cl^- on the southeast side of the cavern increases from 5.10 mol/m^3 to 5.13 mol/m^3 when injecting groundwater into the water curtain system, and it increases from 3.01 mol/m^3 to 3.02 mol/m^3 when injecting freshwater. This shows that adding a vertical water curtain on the southeast side of the cavern group can prevent seawater intrusion as effectively as arranging a vertical water curtain around the cavern group.

The variation in Cl^- concentration along the central axis of Cavern #2 bottom when the vertical water curtain holes extend 10 m, 20 m, and 30 m below the cavern are shown in Figure 24. The maximum Cl^- concentration is 12.4 mol/m^3, 8.4 mol/m^3, and 4.7 mol/m^3, when the holes extend 10 m, 20 m, and 30 m below the cavern, respectively. Therefore, the vertical water curtain system is suggested to extend 30 m from the cavern bottom to meet the requirements for a safe oil storage cavern for 50 years.
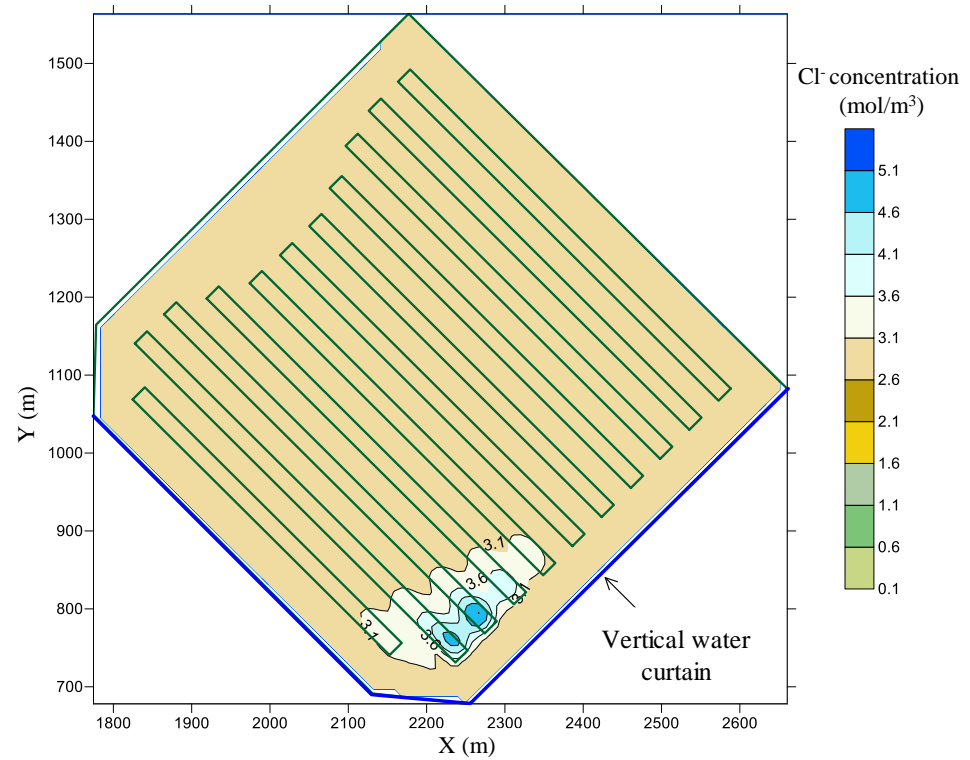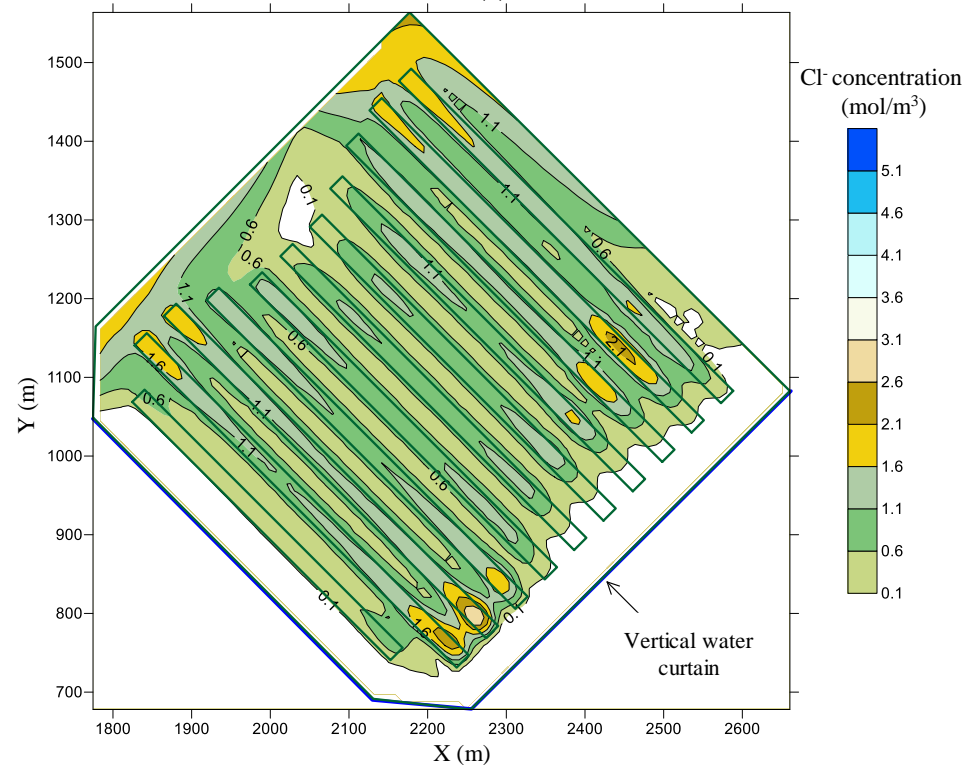
Figure 23. Cl$^-$ concentration at the cavern bottom after 50 years when vertical water curtain is only applied at the southeast of the cavern group: (**a**) groundwater injected into the water curtain system: (**b**) freshwater injected into the water curtain system.
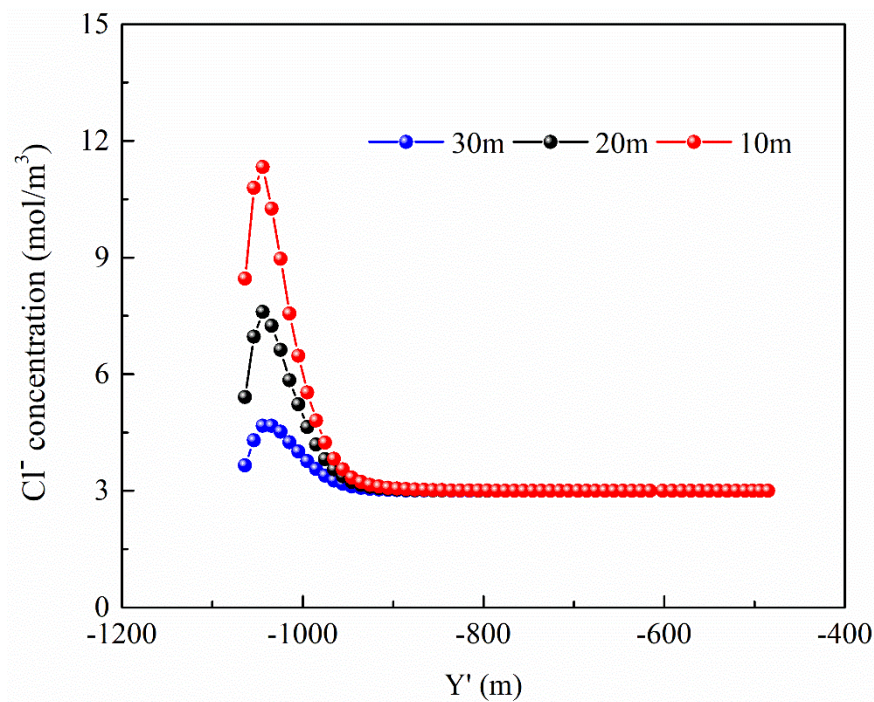
Figure 24. Cl$^-$ concentration along the central axis of the Cavern #2 bottom with different vertical water curtain depths.

5. Conclusions

Seawater intrusion is one of the important issues to address when developing an underground oil storage cavern in a littoral environment. Cl$^-$ in seawater can corrode structures and facilities, reducing the service life of the cavern. A sophisticated three-dimensional hydrogeological model is built in this work based on a littoral underground oil storage cavern project to estimate seepage field and saltwater intrusion risk in a natural state and in construction and operation periods. Numerical simulation is utilized to study the water inflow law and seawater intrusion prevention technology using a water curtain system. The major findings are summarized below.

(1) The measured water level on the northwest side of the top of the cave is the highest, while it is significantly lower on the southeast side. Based on the inversion of the measurement data, the modeled natural seepage field is obtained as the initial seepage field prior to excavation. There is no threat of saltwater intrusion under natural conditions since the Cl$^-$ concentration in the cavern region is less than 7 mol/m^3.

(2) The water inflows after excavating the top, middle, and bottom levels of the main cavern are 6797 m^3/day, 6895 m^3/day, and 6767 m^3/day, respectively, under realistic permeability coefficient zoning and high tide conditions. The highest water supply from the water curtain during excavation is 6039 m^3/day, which is less than the cavern's water inflow. Although the flow direction close to the cavern is still from inland to the sea, the water level in the reservoir region reduced noticeably throughout the excavation phase, leading to the enhancement of dispersion from seawater to freshwater. This suggests minimal seawater intrusion risk during the excavation period.

(3) The southeast of the reservoir area has the highest seawater invasion risk. When the horizontal curtain system is deployed solely, the Cl$^-$ concentration on the southeast side of the cavern group exceeds 7 mol/m^3 after 18 years of operation, and moderate corrosion occurs in 50 years. If an additional vertical curtain system is implemented on the southeast side of the cavern group, the seawater intrusion can be effectively prevented to extend the cavern's service life.

References

1. Bai, Y.; Zhou, D.; Zhou, P. Modeling and analysis of oil import tariff and stockpile policies for coping with supply disruptions. *Appl. Energy* **2012**, *97*, 84–90. [CrossRef]
2. Dou, M.; Zou, S.; Li, H.; Qing, F.; Huang, F.; Liao, X. Research Status and Prospects of Key Technologies for Underground Water-sealed Oil Storage Cave. *IOP Conf. Ser. Earth Environ. Sci.* **2020**, *508*, 012097. [CrossRef]
3. Makita, T.; Miyanaga, Y.; Iguchi, K.; Hatano, T. Underground oil storage facilities in Japan. *Eng. Geol.* **1993**, *35*, 191–198. [CrossRef]
4. Li, Y.; Zhang, G.; Liu, Y.; Zhou, C. A numerical procedure for modeling the seepage field of water-sealed underground oil and gas storage caverns. *Tunn. Undergr. Space Technol.* **2017**, *66*, 56–63. [CrossRef]
5. Xue, Y.; Li, S.; Qiu, D.; Wang, Z.; Li, Z.; Tian, H.; Su, M.; Yang, W.; Lin, C.; Zhu, J. A new evaluation method for site selection of large underground water-sealed petroleum storage depots. *Sci. China Technol. Sci.* **2015**, *58*, 967–978. [CrossRef]
6. Shi, L.; Zhang, B.; Wang, L.; Wang, H.; Zhang, H. Functional efficiency assessment of the water curtain system in an underground water-sealed oil storage cavern based on time-series monitoring data. *Eng. Geol.* **2018**, *239*, 79–95. [CrossRef]
7. Werner, A.; Bakker, M.; Post, V.; Vandenbohede, A.; Lu, C.; AtaieAshatiani, B.; Simmons, C.Y.; Barry, D.A. Seawater intrusion processes, investigation and management: Recent advances and future challenges. *Adv. Water Resour.* **2013**, *51*, 3–26. [CrossRef]
8. Lee, J.; Cho, B. Submarine groundwater discharge into the coast revealed by water chemistry of manmade undersea liquefied petroleum gas cavern. *J. Hydrol.* **2008**, *360*, 195–206. [CrossRef]
9. Kim, J.; Kim, R.; Lee, J.; Chang, H. Hydrogeochemical characterization of major factors affecting the quality of shallow groundwater in the coastal area at Kimje in South Korea. *Environ. Geol.* **2003**, *44*, 478–489. [CrossRef]
10. Jo, Y.; Lee, J.; Choi, M.; Cho, B. Characteristics of seepage water and groundwater in Incheon Coastal LPG storage cavern. *J. Eng. Geol.* **2010**, *20*, 1–12.
11. Lim, J.; Lee, E.; Moon, H.; Lee, K. Integrated investigation of seawater intrusion around oil storage caverns in a coastal fractured aquifer using hydrogeochemical and isotopic data. *J. Hydrol.* **2013**, *486*, 202–210. [CrossRef]
12. Lee, E.; Lim, J.; Moon, H.; Lee, K. Assessment of seawater intrusion into underground oil storage cavern and prediction of its sustainability. *Environ. Earth Sci.* **2015**, *73*, 1179–1190. [CrossRef]
13. Park, H.; Jang, K.; Ju, J.; Yeo, I. Hydrogeological characterization of seawater intrusion in tidally-forced coastal fractured bedrock aquifer. *J. Hydrol.* **2012**, *446*, 77–89. [CrossRef]
14. Li, S.; Zhang, L.; Ma, X.; Xue, Y.; Jiang, Y. Space-time evolution behaviour of seepage field around a large underground petroleum storage caverns with groundwater curtaining. *Rock. Soil. Mech.* **2013**, *34*, 1979–1986.
15. Cui, S.; Guo, S.; Gao, J. Research on water inflow into underground water sealed cave based on unsaturated flow. *Chin. J. Undergr. Space. Eng.* **2017**, *13*, 746–751.
16. Kharroubi, A.; Farhat, S.; Agoubi, B.; Lakhbir, Z. Assessment of water qualities and evidence of seawater intrusion in a deep confined aquifer: Case of the coastal Djeffara aquifer (Southern Tunisia). *J. Water Supply Res Technol.* **2014**, *63*, 76. [CrossRef]
17. Papadopoulou, M.P.; Dokou, Z.; Karatzas, G.P.; Zahariadi, C.I. *Estimation of Seawater Intrusion Front in a Coastal Karstified System Using a Density-Dependent Flow Approach*; Environmental Hydraulics–Christodoulou & Stamou, Ed.; Taylor & Francis Group: London, UK, 2010.
18. Despina, K.; Maria, K.; Filippos, V.; Pantelis, S.; Stephen, K.; Nikos, L.S. A Transient ElectroMagnetic (TEM) Method Survey in North-Central Coast of Crete, Greece: Evidence of Seawater Intrusion. *Geosciences* **2018**, *8*, 107.
19. Yan, F.; He, T.; Fan, W. Failure Mechanism of Subgrade When Surface Water Infiltrating through Fault and Fissure. In Proceedings of the 2011 International Symposium on Water Resource and Environmental Protection, ISWREP, Xi'an, China, 20–22 May 2011; pp. 426–429.
20. Wang, F.; Jiang, X.; Niu, J. Numerical Simulation for Dynamic Response Characteristics of Tunnel near Fault. *Electron. J. Geotech. Eng.* **2016**, *21*, 5559–5576.

21. Huyakorn, P.; Andersen, P.; Mercer, J.; White, H. Saltwater intrusion in aquifers: Development andtesting of a three-dimensional finite element model. *Water Resour. Res.* **1987**, *23*, 293–312. [CrossRef]
22. Liu, H.; Qiao, L.; Wang, S.; Li, W.; Liu, J.; Wang, Z. Quantifying the containment efficiency of underground water-sealed oil storage caverns: Method and case study. *Tunn. Undergr. Space Technol.* **2021**, *110*, 103797. [CrossRef]
23. Qiu, D.; Fu, K.; Xue, Y.; Li, Z.; Ning, Z.; Zhou, B. Seepage field prediction of underground water-sealed oil storage cavern based on long short-term memory model. *Environ. Earth. Sci.* **2021**, *80*, 561. [CrossRef]
24. Li, Y.; Zhang, B.; Shi, L.; Ye, Y. Dynamic variation characteristics of seawater intrusion in underground water-sealed oil storage cavern under island tidal environment. *Water* **2019**, *11*, 130. [CrossRef]
25. Wang, Z.; Li, W.; Li, Z.; Liu, X.; Liang, J.; Zhong, S. Groundwater response to oil storage in large-scale rock caverns with a water curtain system: Site monitoring and statistical analysis. *Tunn. Undergr. Space Technol.* **2020**, *99*, 103363. [CrossRef]
26. Zhang, B.; Shi, L.; Yu, X.; Qi, S. Assessing the water-sealed safety of an operating underground crude oil storage adjacent to a new similar cavern—A case study in China. *Eng. Geol.* **2019**, *249*, 257–272. [CrossRef]
27. Hosseini, N.; Bajalan, Z.; Khoei, A. Numerical modeling of density-driven solute transport in fractured porous media with the extended finite element method. *Adv. Water Resour.* **2020**, *136*, 103453. [CrossRef]
28. Dai, Y.; Zhou, Z. Steady seepage simulation of underground oil storage caverns based on Signorini type variational inequality formulation. *Geosci. J.* **2015**, *19*, 341–355. [CrossRef]
29. Li, W.; Wang, Z.; Qiao, L.; Liu, H.; Yang, J. Determination of the optimal spacing of water curtain boreholes for underground oil storage from the perspective of percolation theory. *Tunn. Undergr. Space Technol.* **2020**, *97*, 103246. [CrossRef]
30. Xu, Z.; Gao, B.; Li, S.; Zhang, L.; Zhao, S.; Shi, X. A groundwater seal evaluation method based on water inflow for underground oil storage caverns. *Tunn. Undergr. Space Technol.* **2018**, *82*, 265–277. [CrossRef]
31. Xue, Y.; Ning, Z.; Qiu, D.; Su, M.-x.; Li, Z.-q.; Kong, F.-m.; Li, G.-k. A study of water curtain parameters of underground oil storage caverns using time series monitoring and numerical simulation. *J. Zhejiang Univ. Sci. A.* **2021**, *22*, 165–181. [CrossRef]
32. University of Science and Technology Beijing. *Feasibility Study Report of an Underground Oil Storage Cavern*; University of Science and Technology Beijing: Beijing, China, 2020.
33. Mao, C. *Seepage Computation Analysis and Control*; China Water & Power Press: Beijing, China, 2003.
34. Sun, N. *Mathematical Modeling of Groundwater Pollution*; Geological Publishing House: Beijing, China, 1989; pp. 33–37.